QUANTUM AND ATOMISTIC SIMULATION OF MECHANICAL AND ELECTRONIC PROPERTIES OF NANO-MATERIALS

BY

KYOUNGMIN MIN

DISSERTATION

Submitted in partial fulfillment of the requirements
for the degree of Doctor of Philosophy in Mechanical Engineering
in the Graduate College of the
University of Illinois at Urbana-Champaign, 2014

Urbana, Illinois

Doctoral Committee:

- Professor Narayana R. Aluru, Chair
- Professor Harley T. Johnson
- Professor Joseph W. Lyding
- Professor Umberto Ravaioli

ABSTRACT

In our modern scientific society, many new nano-materials are emerging that exhibit outstanding properties, and researchers claim that they have great potential to replace conventional mechanical and electronic devices. It is important to provide comprehensive understanding of these new materials to determine their utility and limitations. State-of-the-art computational schemes (from quantum to atomistic simulation methods) make it possible to investigate nano-materials with respect to their mechanical, electrical, thermal, vibrational, and other properties and characteristics. In this work, we used quantum to atomistic simulations methods such as density functional theory (DFT), molecular dynamics (MD) simulations, and semi-empirical tight binding (TB) method to investigate the mechanical and electrical properties of carbon based materials (graphene, fullerenes) and molybdenum disulfide (MoS_2).

The first material we tested was graphene. Graphene has attracted significant attention for the past ten years because of its extraordinary mechanical and electrical properties. The attractive properties of graphene are currently being explored for a number of applications including nanoelectromechanical systems and nanoelectronics. Mechanical experiments have shown that graphene is the strongest material measured so far, and this opens up opportunities for graphene as a great nanomechanical material. In our work, we examined the mechanical properties of graphene under tensile and shear deformation. Using TB and MD simulations, we computed the modulus of elasticity, fracture strength, and shear fracture strain of zigzag and armchair graphene

structures at various temperatures. We also compared the result of two different methods to test tensile deformation, and results were consistent across both methods. To predict shear strength and fracture shear strain, we also present an analytical theory based on the kinetic analysis. We show that wrinkling behavior of graphene under shear deformation can be significant. We compute the amplitude to wavelength ratio of wrinkles using molecular dynamics and compare it with existing theory. Our results indicate that graphene can be a promising mechanical material under shear deformation.

Our second class of materials tested was fullerene. The encapsulation of a single water molecule inside C60 opens up new opportunities for fabrication of novel electronic systems, such as memories, molecular motors, and mechanical nano-resonators. Specifically, the mechanical and electronic properties change of fullerene structures due to water encapsulation can provide fundamental insights for their applications. We chose to examine the mechanical properties of $H_2O(n)@C60$ under hydrostatic strain and point load using DFT. For mechanical tests, both tension and compression were performed. We found that the bulk modulus and elastic modulus increase as the number of water molecules increase. For fracture behavior, two mechanisms were observed: First, under compression, due to the interaction and bond formation between water and C60, structures with more water molecules begin to exhibit fracture at a lower strain. Second, under tension, fracture is initiated from the bond dissociation of C-C bonds on the C60 surface.

We also report on the electronic properties of water encapsulated fullerenes ($H_2O(n)@C60$, $H_2O(n)@C180$, and $H_2O(n)@C240$) under mechanical deformation using density functional theory (DFT). Under a point load, the change in energy gap of empty and water-filled fullerenes is investigated. For C60 and $H_2O(n)@C60$, the energy gap decreases as the tensile strain increases. For $H_2O(n)@C60$, under compression, the energy gap decreases monotonously while for C60, it first decreases and then increases. Similar behavior is also observed for other empty (C180 and C240) and water-filled ($H_2O(n)@C180$, $H_2O(n)@C240$) fullerene structures. The decrease in energy gap of water-filled fullerenes is due to the increased interaction between water and the carbon wall under deformation.

Finally, we explored the electronic properties of MoS_2 when adsorbed on amorphous HfO_2 using density functional theory. A single-layer MoS_2, which is a semiconducting material with a direct band gap of 1.8 eV, has garnered a lot of attention because it has been shown that the electron mobility of MoS_2 at room temperature is comparable to graphene nano-ribbons. This finding has led to multiple attempts to investigate the mechanical and electronic properties of MoS_2 under various conditions. In this study, we examine the band gap modulation in MoS_2. The defective sites on both MoS_2 and HfO_2 are considered- Mo-, S-, and O-vacancy. O-vacancy in HfO_2 increases interaction between two substrates, and reduces the band gap significantly. It also induces the *n*-type doping effect on MoS_2. Defects on MoS_2 (Mo and S) introduce the finite states in the middle of band gap. In addition, the application of an electric field significantly affects the band gap depending on the direction of the field.

To my family

ACKNOWLEDGMENTS

I would like to thank Professor N. R. Aluru for providing me the opportunity to work with him in the group for Computational Nanotechnology. He always guided me and patiently helped me. Without his full support and excellent guidance, I could not have finished this long journey.

It would never have been possible to finish this Ph. D without my lovely family members. My parents have always believed in me and supported whatever decisions I have made. I just want to tell them how much I love and respect them. Special thanks to my wife, Eun Sul Lee, for her love and encouragement, and to Jaewon, my precious son; he has always brought a big smile and happiness to our home and made me enjoy life.

I also would like to express my appreciation to my outstanding co-workers, Prof. Lyding, Prof. Salehi-Khojin, Prof. Zhao, and Prof. Silberstein. They have always been open to fruitful discussions and shared their strengths with me.

I would like to thank the members of the Computational Nanotechnology group, especially Namjung, Joonho, Amir, and Tarun for being good friends and helpful discussion partners.

TABLE OF CONTENTS

CHAPTER 1

INTRODUCTION

Nanoscale, materials demonstrate fundamentally different physical properties which are not observed/considered in the bulk materials. The novel properties exhibited at this scale have garnered a lot of interest in the research community.[1, 2] These nanomaterials exhibit superior properties including-mechanical, electronic, thermal, and vibrational as compared to conventional materials. As a result, they are expected to replace conventional materials in existing micro to macroscale devices, lowering costs and raising efficiency in sensors, actuators, semi-conducting devices, and more. In light of this, there have been many attempts to investigate the fundamental physical/material properties of nanomaterials. However, difficulties in fabrication and construction of nano-scale devices have meant that there were considerable barriers to investigate and comprehensively understand the material properties.

Over the past ten years, there has been rapid growth in computational resources. This has made it possible for researchers to investigate material properties simultaneously under several conditions in nano- to micro-scale devices. In addition, many state-of-the-art quantum to atomic simulation methods have been proposed that are designed to predict material properties accurately and efficiently.[3-6] By utilizing computer simulations, it is possible to study important factors which affect the material properties significantly, i.e. size, defects, surface orientation, and various thermodynamic states.

In this dissertation, exceptional nanomaterials are investigated, which are expected to have promising properties that can contribute significantly to the development of innovative nanotechnology. I used quantum to atomistic simulations methods such as density functional theory (DFT), molecular dynamics (MD) simulations, and semi-empirical tight binding (TB) method to investigate the mechanical and electrical properties of carbon based materials (graphene, fullerenes) and molybdenum disulfide (MoS_2). This dissertation is organized as following:

In Chapter 2, the mechanical properties of graphene under tensile and shear deformation are investigated. The graphene is shown to be stronger than any other material examined thus far under tension.[1] It also has great electron mobility that would be advantageous in applications for numerous nanoelectromechanical devices. This study also includes detailed analyses on size, chirality and temperature effects under mechanical deformation as well as fracture behaviors. The TB method is employed to test tensile properties such as Young's Modulus and Poisson's ratio and results are compared to those obtained from MD simulations. Graphene nanoribbons are also investigated for size effect on tensile properties. For shear properties, MD simulations are performed and their results are compared to the continuum based theory. The wrinkling formation and behaviors of graphene under shear deformation are also studied as these affect the mechanical response significantly.

Chapter 3 addresses the class of materials known as fullerenes. The mechanical properties of water filled C60 (buckyball) are studied using DFT simulation. The encapsulation of a single water molecule inside C60 is achieved by previous experiment and this opens up new opportunities for the fabrication of novel mechanical and electronic devices.[7] For example, by inserting water filled C60 into polymer (polymer composites), one can enhance the mechanical properties significantly. For this study, two different type of loadings, a point load and hydrostatic strain, were applied, and elastic and fracture properties of water filled C60 (with up to 4 water molecules) was studied. We also addressed the limitations of current simulation methods (MD and DFT) and atomic potential dependency for applying mechanical deformation on nanostructures.

In Chapter 4, the energy gap modulation of water filled fullerenes (C60, C180, C240) are investigated under mechanical deformation using DFT calculations. Fullerenes have an energy gap which can be affected by the type of molecules inside, and this can be used as a characteristic property to distinguish the encapsulated material. In addition, this energy gap can be greatly affected by the external mechanical deformation. The effect of mechanical stimuli on the electronic properties of fullerenes and water-filled fullerenes' is still unknown. So understanding these effects can provide new insights for applications such as molecular sensing devices.

In Chapter 5, I address the electronic properties of MoS_2 when adsorbed on amorphous HfO_2. The band gap of a single-layer MoS_2 on a-HfO_2 is investigated using MD and DFT simulations. MoS_2 exhibits a direct band gap of 1.8 eV, and its electron mobility is comparable to the armchair graphene nanoribbon. This means that MoS_2 could be a great material for the application of the field effect transistor (FET).[2] In addition, MoS_2 is expected to have great potential in bio-sensing devices due to its large surface-volume ratio.

The band gap of MoS_2 can be affected from the interaction between deposited dielectric substrate in FET. In this study, the band gap change due to configuration change (defects in MoS_2 and a-HfO_2) on a-HfO_2 is investigated. In addition, the electric field effect is studied to show how the doping effect under applied voltage on both MoS_2 and a-HfO_2 structures can significantly modify the electronic structures of the system.

In Chapter 6, I summarize the findings and conclude with a discussion of the significance of this work.

CHAPTER 2

MECHANICAL PROPERTIES OF GRAPHENE

2.1. Introduction

Graphene has attracted significant attention from the scientific community because of its extraordinary mechanical and electrical properties. The attractive properties of graphene are currently being explored for a number of applications including nano-electro-mechanical systems (NEMS), and nano-electronics. Recent mechanical experiments have shown that graphene is the strongest material measured so far.[1] This opens up opportunities for graphene as a nano-mechanical material.

The mechanical properties of graphene under tension have been investigated extensively using both experiments and atomistic simulation methods. [1, 8-12] On the experimental side, Blakslee *et al.*[13] reported the Young's modulus of bulk graphite to be 1.06 TPa. In addition, Frank *et al.*[8] measured the Young's modulus of a stack of graphene sheets (less than five layers) to be 0.5 TPa. More recently, by nanoindenting the center of a free-standing monolayer graphene membrane with an atomic force microscope, Lee *et al.*[1] measured the Young's modulus as 1.0 ± 0.1 TPa assuming the thickness of graphene to be 0.335 nm. They also reported the intrinsic breaking strength of graphene as 130 ± 10 GPa.

Many theoretical and computational studies have been performed to investigate the mechanical properties of graphene. By using density functional theory with a local density approximation, Liu *et al.*[9] computed the Young's modulus and Poisson's ratio of graphene as 1.050 TPa and 0.186, respectively. Liu *et al.* also reported the maximum Cauchy stress for a uniaxial tensile test in the armchair and zigzag direction (see Figure 2.3) to be 110 and 121 GPa, respectively. Various *ab initio* calculations on graphene reported Young's modulus values of 1.11 TPa[12] and 1.24 TPa[14]. By using the semi-empirical, non-orthogonal tight-binding (TB) method, Hernandez *et al.*[15] reported the Young's modulus of graphene to be 1.206 TPa. Molecular Dynamics (MD) simulation has also been used to compute the mechanical properties of graphene. For example, Young's modulus of graphene was computed to be 1.272 TPa[16] with the modified Brenner potential and 1.026 TPa[17] with reactive empirical bond order (REBO) potential. With the molecular mechanics theory, the Young's modulus of graphene was computed as 0.95 and 1.06 TPa.[18]

The shear modulus of graphene has been also reported using various approaches. By using the molecular mechanics method, Sakhaee-Pour reported the shear modulus of zigzag and armchair structures to be 0.213 TPa and 0.228 TPa, respectively. [19] Zakharchenko *et al.* reported the temperature dependent shear modulus using Monte Carlo simulation, and the highest value is 0.493 TPa at 700 K assuming the thickness of graphene to be 3.335 Å. [20] Tsai *et al.* reported the shear modulus of graphene as 0.358 TPa at 0 K using molecular dynamics with AMBER force field. [21]

Though the shear modulus of graphene has been reported using several approaches, the strength and fracture strain of graphene under shear have not been reported so far. To understand the merits and limitations of graphene as a mechanical material, it is important to look at shear properties of graphene and other materials. McSkimin *et al.* reported the shear modulus of diamond as 0.478 TPa. [22] Roundy *et al.* reported the shear strength of carbon diamond structure as 93 GPa. [23] Zhang *et al.*, using the first-principles approach and the local-density-approximation (LDA), reported the shear strength of c-BN and BC_2N_{-2} as 70.5 GPa and 68.8 GPa, respectively. [24] Shear modulus of graphite was reported to be 0.44±0.03 TPa by Blakslee *et al.* [13] For carbon nanotubes, Lu, using empirical lattice dynamics, reported the shear modulus as 0.45 TPa, Hall *et al.* reported the shear modulus using experiments as 0.41±0.36 TPa, and Lu *et al.* reported the shear strength to be between 41 ~ 54.4 GPa depending on the chirality. [25-27]

Since graphene is a thin membrane structure, it is also important to understand the wrinkling behavior under shear deformation. In related work, Wong *et al.* studied the wrinkling behavior of aluminized Kapton membrane extensively using experiments, and analytical and numerical simulations. Wang *et al.* investigated the wrinkling behavior of graphene under a point load. [28, 29] In summary, experimental and theoretical studies have consistently predicted that graphene has exceptional mechanical properties.

The methods of analysis reported above give us valuable insight into the properties of graphene; however, there are limitations for the use of empirical and *ab initio* simulations. Though empirical methods are good for obtaining properties of bulk materials without any structural defects, they are not sufficiently accurate and they show high levels of potential dependency which results in limited transferability for calculating material properties. On the other hand, *Ab initio* methods can describe the quantum-mechanical nature of the atomic cohesion very accurately, but due to the limited computational resources, the size of the system needs to be in the range of a few angstroms, and it cannot be generally used to investigate material properties for a wide variety of applications. These limitations led us to use the alternative method that follows, which can provide reasonable accuracy comparing to the empirical methods but computationally more efficient than *Ab initio* method.

2.2. Tight Binding Method[5, 30]

The Tight Binding (TB) method is a quantum mechanical model that can be applied to determine the ground state energy of the atomic structures and the properties of materials. The advantages of using TB model are: a) it is based on the quantum mechanical nature of the subject, so this model can be applied to various materials under different conditions; and, b) it is a relatively simple model compared to the *ab initio* method, so it is computationally efficient.

2.2.1 Band structure energy and Repulsive terms

To compute the ground state energy of the system using the TB method, the following steps are employed. First, based on the initial configuration of the system, a Hamiltonian matrix of the system is constructed using a Slater and Koster table. The example of Hamiltonian matrix including two graphene atoms a and b is shown in Figure 2.1.

$$H^0 = \begin{bmatrix}
h_{a,a}^{ss} & 0 & 0 & 0 & h_{a,b}^{ss} & h_{a,b}^{sp_x} & h_{a,b}^{sp_y} & h_{a,b}^{sp_z} \\
0 & h_{a,a}^{p_x p_x} & 0 & 0 & h_{a,b}^{p_x s} & h_{a,b}^{p_x p_x} & h_{a,b}^{p_x p_y} & h_{a,b}^{p_x p_z} \\
0 & 0 & h_{a,a}^{p_y p_y} & 0 & h_{a,b}^{p_y s} & h_{a,b}^{p_y p_x} & h_{a,b}^{p_y p_y} & h_{a,b}^{p_y p_z} \\
0 & 0 & 0 & h_{a,a}^{p_z p_z} & h_{a,b}^{p_z s} & h_{a,b}^{p_z p_x} & h_{a,b}^{p_z p_y} & h_{a,b}^{p_z p_z} \\
h_{a,b}^{ss} & h_{a,b}^{p_x s} & h_{ab}^{p_y s} & h_{ab}^{p_z s} & h_{b,b}^{ss} & 0 & 0 & 0 \\
h_{a,b}^{sp_x} & h_{a,b}^{p_x p_x} & h_{a,b}^{p_y p_x} & h_{a,b}^{p_z p_x} & 0 & h_{b,b}^{p_x p_x} & 0 & 0 \\
h_{a,b}^{sp_y} & h_{a,b}^{p_x p_y} & h_{a,b}^{p_y p_y} & h_{a,b}^{p_z p_y} & 0 & 0 & h_{b,b}^{p_y p_y} & 0 \\
h_{a,b}^{sp_z} & h_{a,b}^{p_x p_z} & h_{a,b}^{p_y p_z} & h_{a,b}^{p_z p_z} & 0 & 0 & 0 & h_{b,b}^{p_z p_z}
\end{bmatrix}$$

Figure 2.1: Hamiltonian matrix for atom a and b

In a Hamiltonian matrix, diagonal terms are onsite energies for each atomic orbitals, and the other terms are the hopping integrals between two atoms. It should be noted that the orbitals on the same atom are orthogonal. To compute the band structure energy, the Hamiltonian matrix is solved using eigensolver, and the sum of electronic eigenvalues over all occupied electronic states is calculated. For carbon, onsite energies, hopping integrals, and the other model parameters are developed by Xu *et al*.[5] The short-ranged repulsive terms for the system are calculated based on the pairwise potential which is dependent on the cut-off radius of the considered system.[5] The ground state energy of a single layer of graphene is computed as a function of the first nearest carbon-carbon distance in Figure 2.2.

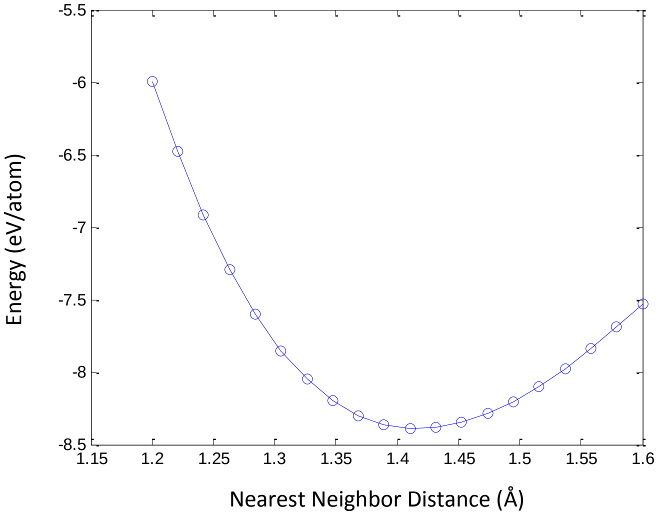

Figure 2.2: Ground state energy vs. Nearest neighbor distance for graphene

2.3. Size and Chirality Dependent Elastic Properties under Tensile Deformation

2.3.1 Methods

In this study, we investigate the size and chirality effects on the elastic properties of graphene nanoribbons the orthogonal tight binding (TB) method.[5] As shown in Figure 2.3, we investigate the mechanical properties of approximately square-shape graphene nanoribbons in both the armchair direction and the zigzag direction. In particular, we investigate the size and chirality dependence of Young's modulus of graphene nanoribbons and bulk graphene

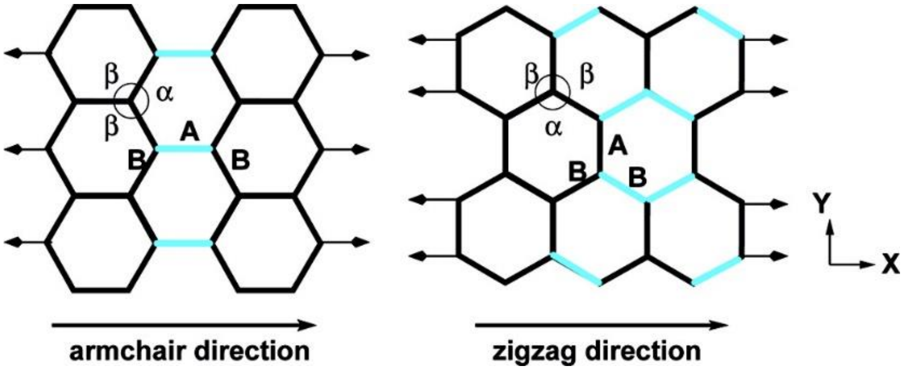

Figure 2.3: A graphene nanoribbon with (a) armchair edges and (b) zigzag edges.[1]

We have used the orthogonal tight-binding method to calculate the Young's modulus of graphene with the parameters proposed by Xu *et al.*[5] For a *N* atom system, with the relaxed atomic configuration, the total energy (E_{Total}) can be calculated by $E_{Total}=E_{bs} + E_{rep}$, where E_{bs} is the sum of electronic eigenvalues over all occupied electronic states obtained by solving an empirical tight-binding Hamiltonian, and E_{rep} is the sum of the repulsive energy calculated from the scaling function and the pairwise potential.[5] The Young's modulus (Y) of the system in the *x* direction can be obtained from the elastic constants[31] as (assuming graphene to be an orthotropic material)

---

[1] Note that Figure 2.3 is generated by Huijuan Zhao (*Nano Letters* 2009, 9, 3012-3015)

$$C_{ijkl} = \frac{\partial^2 W_T}{\partial F_{ij} \partial F_{kl}} - \frac{\partial^2 W_T}{\partial F_{ij} \partial \xi_m} \left(\frac{\partial^2 W_T}{\partial \xi_m \partial \xi_n} \right)^{-1} \frac{\partial^2 W_T}{\partial \xi_n \partial F_{kl}} \quad (2.1)$$
$$i, j, k, l, m, n = x, y, z$$

$$Y = \frac{C_{xxxx} C_{yyyy} - C^2{}_{xyxy}}{C_{yyyy}} \quad (2.2)$$

where $W_T = E / V_0$ is the energy density, V_0 is the initial volume of the relaxed structure, F is the Green-Lagrange strain tensor, and ξ is the inner displacement between the two Bravais lattices of the graphene structure.

2.3.2 Results

To investigate the effect of chirality on the mechanical properties of bulk graphene, we perform TB simulations. Young’s modulus in both armchair and zigzag directions is calculated using the relaxed configuration of a 680 atom graphene lattice with PBC. The Young’s modulus (Y_b) 0.91 TPa from the TB simulation, which is consistent with previous references.

Then, the size and chirality effect on the mechanical properties of graphene nanoribbons are investigated. Graphene nanoribbon structures are first relaxed to minimize the energy, and the Young’s modulus is calculated for armchair and zigzag directions using the method described above. In parts (a) and (b) of Figure 2.4, we plot the variation of normalized Young’s modulus (Y / Y_b) as a function of the size of the graphene nanoribbon. We observe that Young’s modulus along armchair and zigzag directions increases with the diagonal length of the nanoribbon and slowly converges to the Young’s modulus of bulk graphene, whereas the Poisson’s ratio decreases

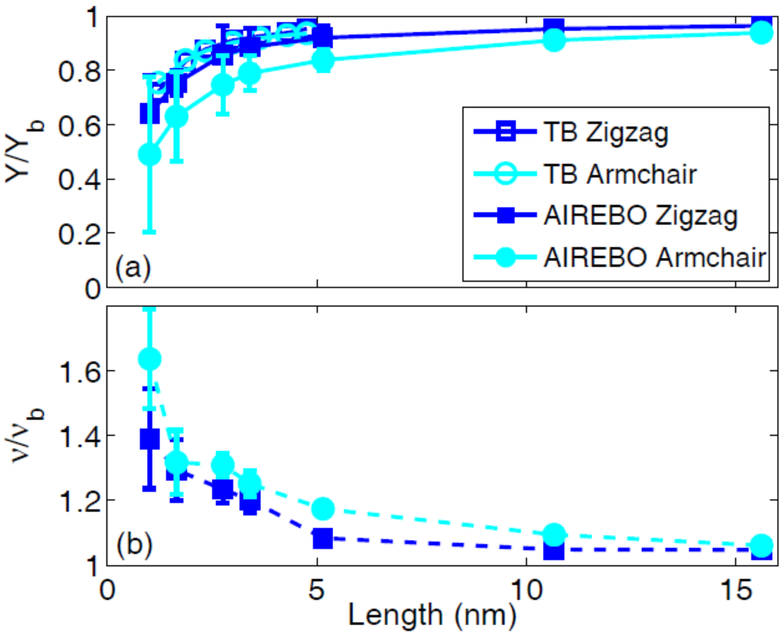

Figure 2.4: Normalized Young's modulus (Y/Y_b) (a) and normalized Poisson's ratio ν/ν_b (b) as a function of the graphene nanoribbon's diagonal length for uniaxial tension along the armchair and zigzag directions[2].

with the increase in diagonal length of nanoribbon and converges to the bulk value. This variation is similar to the size-dependent Young's modulus of a carbon nanotube, even though the Young's modulus and Poisson's ratio show more size dependence in the two-dimensional graphene nanoribbon structure compared to the one-dimensional carbon nanotube structure.[32] For example, the size effect on Young's modulus is negligible when the diagonal length of the graphene nanoribbon is over 10.0 nm. However, the size effect can be neglected when the diameter of the carbon nanotube is larger than 0.75 nm. TB simulations do not indicate any significant dependence of Young's modulus and Poisson's ratio on chirality. However, MD simulations indicate significant chirality effects. For the same size nanoribbon, Young's modulus is larger along the

---

[2] Note that MD results in Figure 2.4 is computed by Huijuan Zhao (*Nano Letters* 2009, 9, 3012-3015)

zigzag direction than along the armchair direction, whereas Poisson's ratio is larger in the armchair direction than in the zigzag direction. The differences in MD and TB simulation results are due to the different parameters and potentials used in the models. For instance, MD simulations are carried out at room temperature with thermal fluctuations involved in the out-of-plane direction, while TB simulations are carried out at zero-temperature with a perfect two-dimensional lattice structure. The results also suggest that potentials in MD and TB simulations need to be understood in more detail for graphene. It is also important to note that both MD and TB simulations predict similar magnitude for the size dependence, which is much larger than the prediction[32] made by the continuum mechanics approximation with the Tersoff-Brenner potential.[33] In this approach, the Young's modulus of the graphene nanoribbon is calculated based on a two-dimensional equilibrium configuration (no rippling) with the assumption of straight edges by directly minimizing the potential energy.

2.4. Size and Chirality Dependent Shear Properties

In this work, we perform extensive molecular dynamics simulations to understand the shear modulus, shear strength and fracture strain of graphene as a function of temperature and chirality. Furthermore, we also investigate the wrinkling of graphene under shear deformation using molecular dynamics and analytical theory. [28] We also present an analytical theory based on the kinetic analysis to compute the shear strength and strain and compare the results with those obtained from molecular dynamics simulations. The rest of the paper contains details on molecular dynamics simulations, analytical theory based on kinetic analysis for fracture of graphene, and results on mechanical properties of graphene under shear deformation.

2.4.1 Methods

Molecular dynamics (MD) simulations are performed using LAMMPS[34] with the adaptive intermolecular reactive empirical bond order (AIREBO) potential[6]. It has been shown that the AIREBO potential can accurately compute the bond-bond interaction, bond breaking, and bond reforming in the carbon atoms. [10, 11] To capture the fracture behavior accurately and to avoid non-physical phenomenon, the cutoff parameter is modified as 2.0 Å for the REBO part of the potential. [35]

To compute the shear properties of bulk graphene, a total of 3936 carbon atoms with a size of 100.8 Å x 102.2 Å and with periodic boundary conditions, is initially relaxed using NPT simulation until the energy of the system is fully minimized for each specified temperature in the range of 100 K ~ 2000 K. The thickness of graphene is assumed to be 3.335 Å. We implement the deformation-control method by applying the shear strain rate of 0.001 ps^{-1} to bulk graphene (for both zigzag and armchair cases, separately). [11] The strain increment is applied after every 1000 time steps using NVT simulation. The Velocity-Verlet time stepping scheme is used with a time step of 0.1 fs and Nosé-Hoover thermostat is used for temperature control.

Shear modulus, G, is computed using the expression,

$$G = \frac{1}{V_0}\left(\frac{\partial^2 E}{\partial \gamma_{xy}^2}\right)_{\gamma_{xy}=0} \tag{2.3}$$

where E is the strain energy, V_0 is the volume, and shear strain, $\gamma_{xy} = \Delta x / L$, where Δx is the transverse displacement and L is the initial length of graphene. To verify the shear modulus calculation, the linear portion of the shear stress and strain curve is used, $G = \tau_{xy}/\gamma_{xy}$, where τ_{xy}

is the shear stress at 0.005 strain. This result is consistent with the result obtained from the strain energy based method described above.

The analytical theory employed here is based on the kinetic analysis of fracture. In kinetic analysis, the fracture of a material (lifetime of the fracture of a solid) is determined by two dominant factors, mechanical stress and temperature, i.e.,

$$\tau = \tau_0 \exp\left(\frac{U_0 - \beta\tau_{xy}}{kT}\right) \tag{2.4}$$

where τ_0 is the vibration period of atoms in a solid, which is taken[36] to be 10^{-13} s, T is the temperature, U_0 is the inter-atomic bond dissociation energy, β = qV, where V is the activation volume and q is the coefficient of local overstress, and k is the Boltzmann constant. According to the Bailey criterion[37], if the stress varies with time, the fracture is initiated when $\int_0^{t_f} \frac{dt}{\tau[T,\ \tau_{xy}(t)]} = 1$, where t_f is the time to fracture, and $\tau_{xy}(t)$ is the time- dependent stress.

To capture the nonlinear shear stress and strain behavior, a nonlinear expression relating shear stress to shear strain is employed, i.e., $\tau_{xy}(t) = a\ln[b\gamma_{xy}(t) + 1.0]$. Assuming a constant strain rate, $\dot{\gamma}_{xy}$, the nonlinear stress-strain expression is given by

$$\tau_{xy}(t) = a\ln[b\dot{\gamma}_{xy}t + 1.0] \tag{2.5}$$

Then, $\tau_f = a\ln[b\dot{\gamma}_{xy}t_f + 1.0]$ is defined as the fracture stress. Substituting Eq. (2.5) and the expression for the life time (τ) into the Bailey criterion, we can obtain the temperature-dependent expression for fracture stress as,

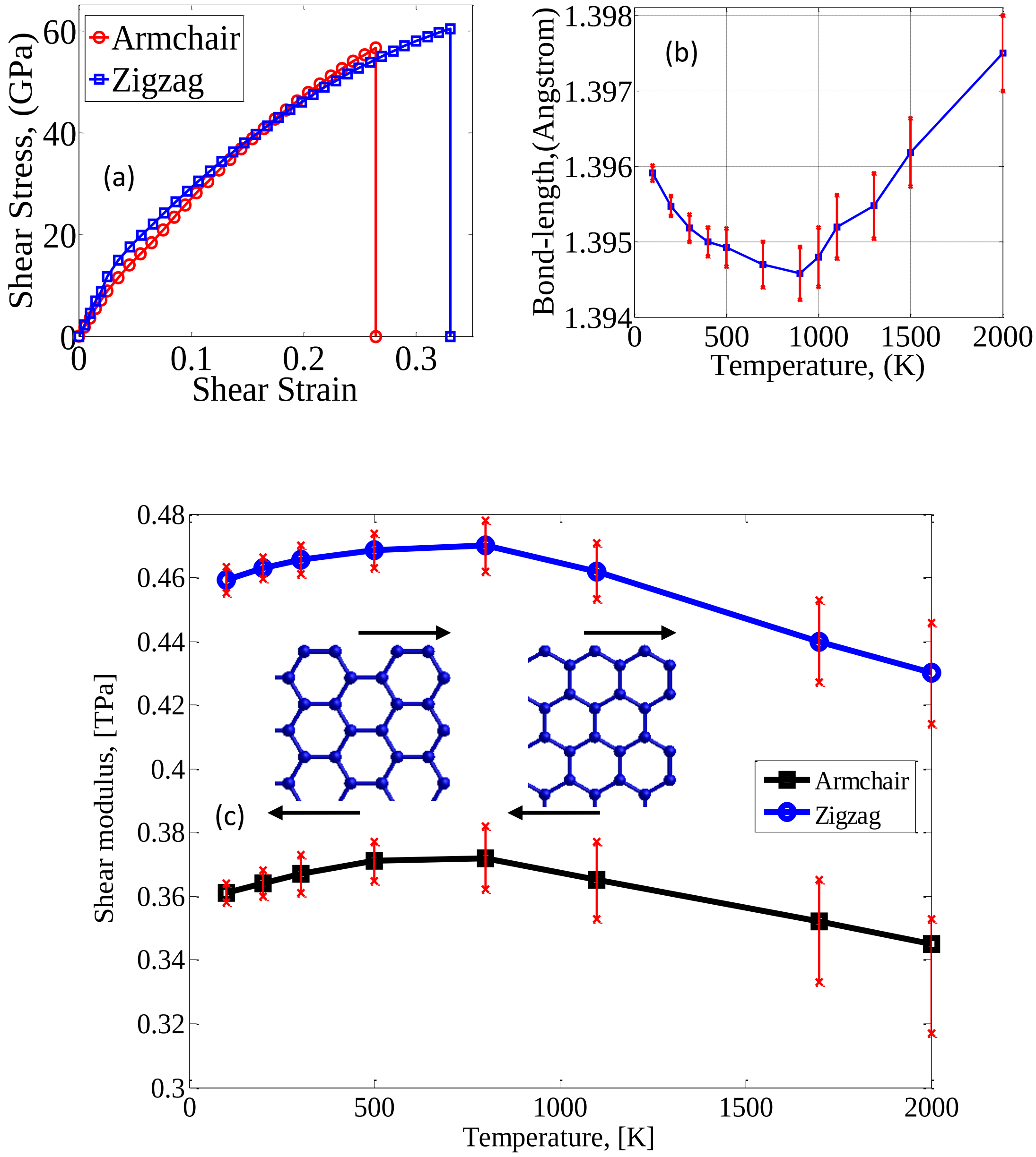

Figure 2.5: (a) Shear stress vs strain curve at 300 K. (b) First nearest C–C bond-length vs. temperature. (c) Chirality and temperature-dependent shear modulus. (Inset: armchair and zigzag graphene configuration for shear tests).

$$\tau_f(\dot{\gamma}_{xy},\ T)=\frac{akT}{\beta a+kT}\left[\frac{U_0}{kT}+\ln\left(b\dot{\gamma}_{xy}\tau_0\left(\frac{\beta a}{kT}+1\right)\right)\right] \tag{2.6}$$

Furthermore, the expression for fracture strain is given by

$$\gamma_f=\frac{1}{b}\left[\exp\left(\frac{\tau_f}{a}\right)-1.0\right] \tag{2.7}$$

The inter-atomic bond dissociation energy, activation volume, and the parameters a and b do not vary significantly with temperature. The values used for these parameters for zigzag and armchair structures are summarized in Table 2.1.

	U_0 [eV]	V [Å ^{3}]	a [10^{11} Pa]	b
Zigzag	1.85	4.69	0.44	9.3
Armchair	1.77	4.56	0.63	5.5

TABLE 2.1: Parameters for Kinetic Analysis

2.4.2 Shear Stress and Strain curve

Shear stress as a function of shear strain for zigzag and armchair graphene are obtained for various temperatures. As shown in Figure 2.5, for both armchair and zigzag cases, as the temperature increases, the shear modulus increases at first and then starts to decrease as the temperature increases beyond 800 K. As shown in inset 3 in Figure 2.5, the anomalous variation of the shear modulus can be explained by the anomalous variation of the bond-length with temperature. As the bond-length increases, the intermolecular interactions become weaker resulting in a decrease in shear modulus and vice versa. The bond-length variation with temperature is in reasonable agreement with the result obtained using Monte Carlo simulation. [20] Zigzag graphene shows a slightly higher shear modulus compared to the armchair graphene. As shown in inset 2 of Figure 2.5, the shear stress versus strain curve shows a bifurcation point (change in slope) for a shear strain of around 0.024 for both chiralities. The critical shear stress when wrinkles appear at the bifurcation point is 10.5 GPa and 8.7 GPa for zigzag and armchair structures, respectively, at 300 K. The decrease in slope represents a softening of the material (lower shear modulus). Beyond the bifurcation point, the wrinkles in the graphene membrane start to grow and the amplitude of the wrinkles becomes higher.

2.4.3 Wrinkling Behavior

Since wrinkles can affect the mechanical behavior of graphene, we investigate the growth of wrinkles (in particular the amplitude and wavelength) under shear deformation. The ratio of the amplitude to the wavelength of wrinkles at various temperatures can be computed directly from the molecular dynamics data. In addition, the ratio can also be computed using theory [28, 38] as,

$$\frac{A}{\lambda} = \frac{\sqrt{2(1-\upsilon)\gamma_{xy}}}{\pi} \tag{2.8}$$

where A is the amplitude, λ is the half-wavelength, υ is Poisson's ratio, and γ_{xy} is the shear strain. The derivation of this analytical model based on that the amplitude of wrinkle is obtained from the total transverse strain, which is the sum of the strain in the membrane (Poisson's ratio effect) and the out-of-plane deformation.[38]

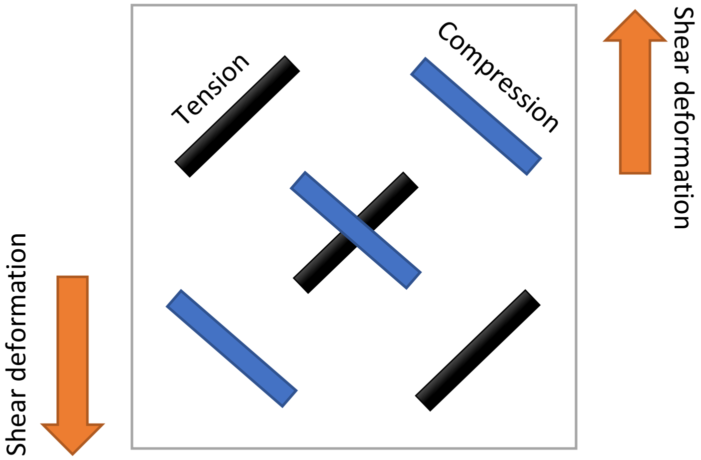

Figure 2.6: Wrinkling formation under shear deformation

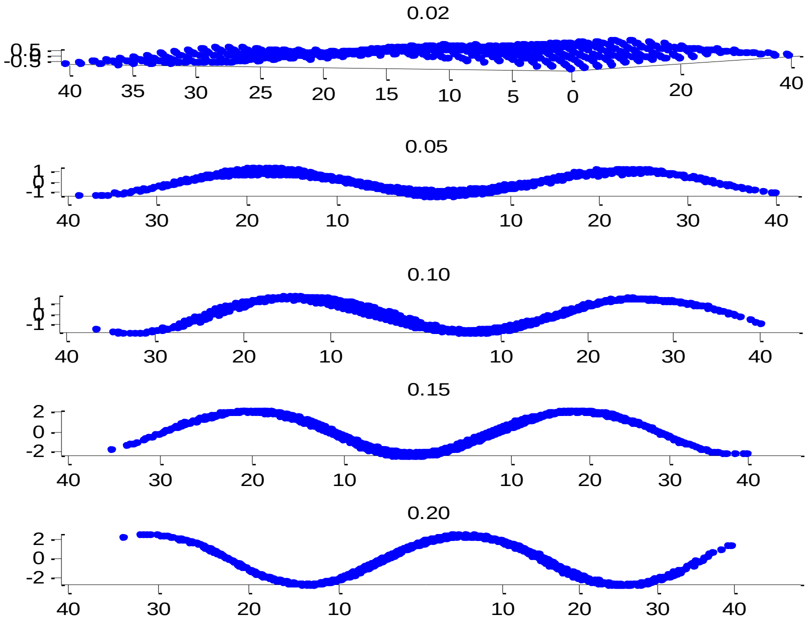

Figure 2.7: The side view of wrinkling in graphene as the shear strain increases

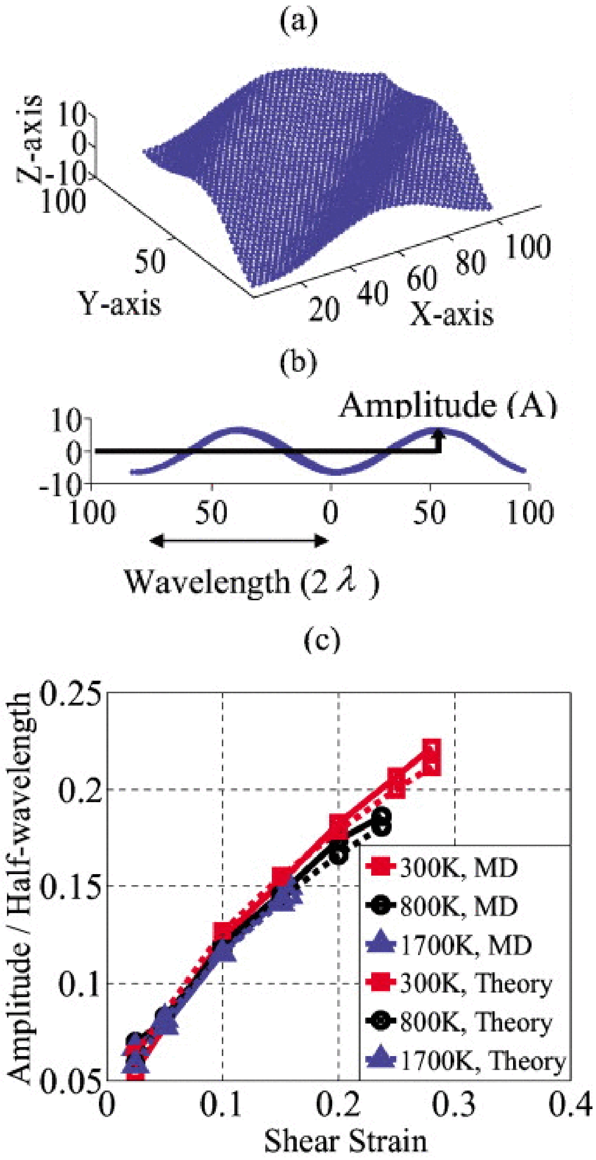

Figure 2.8: Wrinkle structures in graphene. (a) Wrinkles in zigzag graphene at 0.2 strain, 300 K. (b) Side view of wrinkles. (c) Ratio of amplitude to half-wavelength vs shear strain at different temperatures for zigzag graphene and comparison with the analytical expression.

For the Poisson’s ratio, we take a value of 0.21 ± 0.01 at 300 K[10], 0.32 ± 0.08 at 800 K, and 0.34±0.11 at 1700 K. We note that the ratio of the amplitude to the half-wavelength is not strongly dependent on the chirality of the graphene structure. This is reasonable because the Poisson’s ratio for both chiralities is approximately the same.

The comparison between MD and theory is shown in Figure 2.8. We note that the comparison is reasonable. Understanding the role of wrinkles is important, especially in a material like graphene, as wrinkles can lead to the softening of the material. To demonstrate the significance of wrinkles, we performed shear test on the zigzag graphene using molecular dynamics and preventing the formation of wrinkles by maintaining the force component in the out-of-plane (z-direction) as zero. The fracture stress of a flat graphene sheet (with no wrinkles) is 97.54 GPa at 300 K, which is about 37 GPa higher when wrinkles are taken into account.

2.4.4 Temperature effect- Fracture behaviors

We also performed fracture simulations on zigzag and armchair graphene structures under shear deformation at various temperatures. The shear strength and shear fracture strain of armchair and zigzag structures as a function of temperature are shown in Figure 2.9. We note that both the shear strength and the fracture strain decrease as temperature increases. The decrease in strength can be explained by larger thermal fluctuations at higher temperatures. The chirality effects are more clearly observed at lower temperature and are not that significant at higher temperatures. In particular, zigzag graphene shows a slightly higher strength at lower temperatures compared to the armchair graphene. We note that the fracture of graphene is initiated when the bonds along the north-west diagonal direction start to break because of the shear force.

In Figure 2.9, we also show the results from analytical theory based on kinetic analysis. While the results from the analytical theory compare reasonably well with MD data for both fracture stress and fracture strain, the chirality effects are not clearly observed with the analytical theory. Our results indicate that the shear strength of graphene at 300 K is higher compared to that of the CNT case (41 ~ 54.4 GPa) [27] , and lower compared to that of carbon diamond (93 GPa) [23], c-BN (70.5 GPa) and BC2N-2 (68.8 GPa)[24].

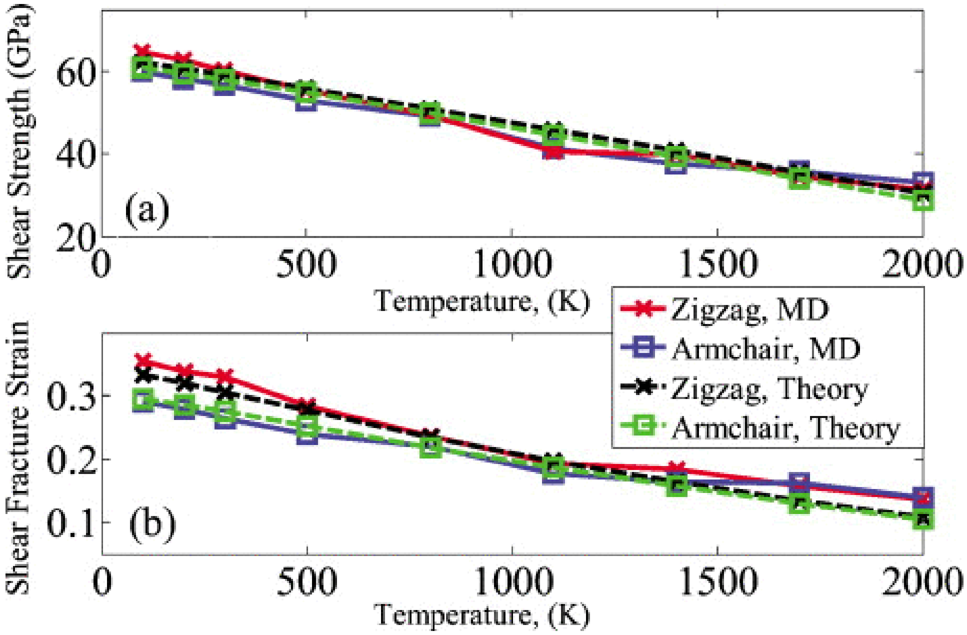

Figure 2.9: Chirality and temperature-dependent shear strength and shear fracture strain and comparison with kinetic analysis of the mechanism of fracture.

2.5. Conclusion

In summary, we have performed an extensive study to understand the size and chirality effects on the elastic properties of graphene nanoribbons. The predicted Young's modulus for bulk graphene are in reasonable agreement with the published theoretical[9] and experimental[1] data. The stiffness decreases when the size of graphene nanoribbon decreases. Two dimensional graphene nanoribbons exhibit a larger size dependence on the mechanical properties compared to the one-dimensional carbon nanotubes.

We also investigated the temperature and chirality dependent shear properties of graphene using molecular dynamics simulations. Our results indicate that shear modulus increases up to around 800 K and decreases as the temperature is increased further. Shear strength and fracture strain decrease as the temperature is increased. Zigzag graphene shows a higher shear modulus compared to the armchair structure. The shear fracture strength and shear fracture strain for the zigzag case are higher compared to the armchair case at lower temperatures, and no significant difference is observed at higher temperatures. We showed that analytical theory based on kinetic analysis compares reasonably with MD data. Finally, we also investigated wrinkling of graphene under shear deformation and since wrinkling can affect mechanical properties, this needs to be carefully accounted for when exploring applications based on graphene.

CHAPTER 3

MECHANICAL BEHAVIOR OF WATER FILLED C60

3.1. Introduction

The encapsulation of a single water molecule inside C60 opens up new opportunities for fabrication of novel electronic systems such as memories, molecular motors and mechanical nano-resonators.[7] Similarly, storage of hydrogen, nitrogen, and other molecules becomes feasible inside nanometer systems like C60.[39, 40] Molecular scale confinement can alter the properties of caged molecules. For example, when a single water molecule is encapsulated in C60, the dipole moment of $H_2O@C60$ is about 1/4 of that of H_2O.[41] The vibrational frequencies and rotational motion of a single water molecule are affected by the imprisonment because hydrogen bonding to the other water molecules is restricted by the cage.[42] Graphitic materials such as carbon nanotubes, graphene, and buckyball have been shown to have excellent mechanical properties.[1, 10, 43-45] C60, because of its spherical nature, can enable development of strong composite materials. It has been shown that C60 can enhance the mechanical properties when incorporated inside polymers.[46, 47] On the other hand, insertion of other molecules inside C60 can enhance the mechanical properties of C60. Shen showed that putting Si or Ge inside C60 can increase the mechanical response under compression using Molecular Dynamics (MD) simulations.[48] However, the mechanical behavior of water filled buckyball and the interaction between water and the buckyball surface, which can significantly affect the mechanical response under various loading conditions, have not been studied. Moreover, the origin of mechanical failure due to the presence of water molecules inside C60 is still unknown. The studies performed here on water filled C60 can provide good insights into the application of water filled C60 as agents in composite materials.

In this study, we investigate the effect of water encapsulation on the mechanical properties of C60. We inserted water molecules in C60, and simulated these systems ($H_2O(n)@C60$, n=1, 3, 4, with n being the number of water molecules) using DFT. Two different types of loading, a point load and a hydrostatic strain, are considered. For each type of loading, both compression and tension tests were performed to obtain the mechanical strength of $H_2O(n)@C60$. Due to the spherical nature of C60, interesting mechanical responses were captured under various loading conditions. Bond-dissociation of buckyball and bond-formation between water and C60 are shown to play an important role for the fracture behavior.

3.2. Density Functional Theory (DFT)[3, 49]

3.2.1 Quantum mechanical many-body problem

The properties of materials- structural, electronic, magnetic, optical, and vibrational, consisting of interacting electrons and nuclei, can be investigated by solving the many-body Schrödinger equation in quantum mechanics theory. The many-electron time-independent Schrödinger equation is written as:

$$\hat{H}\Psi = E\Psi \tag{3.1}$$

where $\hat{\mathrm{H}}$ is the Hamiltonian operator, Ψ is the eigenvector, and E is the eigenvalue. The functional forms of $\mathrm{H}\varphi$ can be defined as:

$$\hat{\mathrm{H}} = -\sum_{i} \frac{\hbar^2}{2m_e} \nabla_i^2 - \sum_{i,\alpha} \frac{\mathrm{Z}_\alpha e^2}{\left| \vec{r}_i - \vec{R}_\alpha \right|} + \frac{1}{2} \sum_{i \neq j} \frac{e^2}{\left| \vec{r}_i - \vec{r}_j \right|} - \sum_{\alpha} \frac{\hbar^2}{2M_\alpha} \nabla_\alpha^2 + \frac{1}{2} \sum_{\alpha \neq \beta} \frac{\mathrm{Z}_\alpha \mathrm{Z}_\beta e^2}{\left| \vec{R}_\alpha - \vec{R}_\beta \right|} \tag{3.2}$$

where $\hbar$ is Plank's constant, m_e and M_α are the mass of the electron and the nucleus, respectively. Z_α and Z_β are the atomic number of the α^{th} and β^{th} atom, and e is the electron charge. $\vec{r}_i$ and $\vec{r}_j$ are the position of the i^{th} and j^{th} electron. $\vec{R}_\alpha$ and $\vec{R}_\beta$ are the α^{th} and β^{th} nucleus. The first term is the kinetic energy for the electrons, the second term is the potential for the interaction between electrons and the nuclei, the third term is for the electron-electron interaction, the fourth term is the kinetic energy for the nuclei, and the fifth term is for the nucleus-nucleus interaction.

To reduce the complexity of solving the Schrödinger equation, adiabatic or the Born-Oppenheimer approximation is applied. This approximation can decouple the relation between the electron and nucleus because the mass of nucleus is much heavier than the electron, therefore, the movement of nuclei is much slower than the electron. If one can ignore the dynamics of nucleus, i.e. the nuclear positions are fixed, the description of the wavefunction in Eq. (3.2) for the electron-nucleus can be decoupled. Then the Hamiltonian operator in the Schrödinger equation can be simplified, and arranged as:

$$\hat{\mathrm{H}} = -\sum_{i} \frac{\hbar^2}{2m_e} \nabla_i^2 + \frac{1}{2} \sum_{i \neq j} \frac{e^2}{\left| \vec{r}_i - \vec{r}_j \right|} + V_{ext} \tag{3.3}$$

where the second and the fifth term in Eq. (3.2) is called the external potential, V_{ext}, which is written as $V_{ext} = -\sum_{i,\alpha} \frac{Z_\alpha e^2}{\left|\vec{r}_i - \vec{R}_\alpha\right|} + \frac{1}{2}\sum_{\alpha \neq \beta} \frac{Z_\alpha Z_\beta e^2}{\left|\vec{R}_\alpha - \vec{R}_\beta\right|}$, and this equation assumes that the effect of interaction between nuclei (the second term of V_{ext}) is constant.

Although the dynamics of nuclei can be ignored, it is still complicated to solve the many-body electronic Schrödinger equation because the description of the wavefunctions are all dependent on the electron-electron interactions. Even though the many-body electron wave functions satisfy the many-electron Schrödinger equation, it is almost impossible to calculate the N number of electrons which have 3 × N degrees of freedom and this requires expensive computational resources. In addition, the wavefunction in the many-body problem needs to be solved for each spatial coordinate of the N number of electrons.

3.2.2 Kohn-Sham (KS) theorem

Kohn and Sham proposed the density functional theory (DFT) to reduce and address these limitations. The fundamental concept of DFT is that the ground state of the many-body system can be described with the unique functional form of the single particle electron density instead of describing the many-body wavefunction. This makes the calculation much simpler, but still provides physically reliable results.

The basic framework of DFT is developed by Kohn-Sham (KS) by replacing the many-body Hamiltonian operator with a non-interacting single particle Hamiltonian, and it has been solved for the electronic structure calculation of solids. The ground state energy of the KS equation is written as:

$$E_{KS}[n(\vec{r})] = T_s[n(\vec{r})] + \int d\vec{r} V_{ext}(\vec{r}) n(\vec{r}) + E_{Hartree}[n(\vec{r})] + E_{xc}[n(\vec{r})] \tag{3.4}$$

where $\vec{r}$ is the spatial coordinate, $T_s[n(\vec{r})]$ is the kinetic energy of the non-interacting electron, $V_{ext}(\vec{r})$ is the external potential due to the nuclei charge and any applied external fields, $E_{Hartree}[n(\vec{r})]$ is the classical Coulomb (electrostatic) term (Hartree energy) defined as $E_{Hartree}[n(\vec{r})] = \frac{e^2}{2}\int d^3r d^3r' \frac{n(\vec{r})n(\vec{r}')}{|\vec{r}-\vec{r}'|}$, and $E_{xc}[n(\vec{r})]$ is the exchange-correlation function that addresses the many-body effects.

The Eq. (3.4) can be minimized by the electron density, $n(\vec{r})$, which is the function of electronic wavefunction, and it is defined as:

$$n(\vec{r}) = \sum_i^N f_i |\psi_i(\vec{r})|^2 \tag{3.5}$$

where f_i is the Fermi-Dirac distribution function for describing the distribution of electrons, and $\psi_i(\vec{r})$ is the wavefunction of the electron.

By minimizing the ground state energy functional (E_{KS}) with respect to the electron density ($n(\vec{r})$), one can obtain the following well-known KS equation:

$$\left[-\frac{1}{2}\nabla^2 + V_{eff}(\vec{r})\right]\psi_i(\vec{r}) = \varepsilon_i \psi_i(\vec{r}) \tag{3.6}$$

where the effective potential, $V_{eff}(\vec{r})$, is written as:

$$V_{eff}(\vec{r}) = V_{ext}(\vec{r}) + V_{Hartree}(\vec{r}) + V_{xc}(\vec{r}) \tag{3.7}$$

$$V_{Hartree}(\vec{r}) = \int d^3r' \frac{n(\vec{r}')}{|\vec{r} - \vec{r}'|} \text{ , and } V_{xc}(\vec{r}) = \frac{\delta E_{xc}[n(\vec{r})]}{\delta n(\vec{r})} \tag{3.8}$$

In order to find the solution of the KS equation for the ground-state electron density, the Eq. (3.6) can be solved in the self-consistent steps using the iterative numerical method as shown in Figure 3.1. Since the solution of eigenvector, $\psi_i(\vec{r})$, is dependent on the electron density, the KS equation must be solved self-consistently with the following steps:

(a) First define the trial guess of the electron density, $n(\vec{r})$

(b) Calculate the effective potential, $V_{eff}(\vec{r})$, based on the initial guess of electron density

(c) Solve the KS equation, and obtain the wavefunction and energies

(d) Compute the electron density

(e) Repeat steps (a)-(d) until the electron density reaches the convergence criteria

(f) Compute the desired properties: energy, forces, etc.

It is important to note that the KS theorem uses three major approximations: a) exchange-correlation (XC) functionals to include the many-body effects; b) pseudopotentials for the description of the external potential, $V_{ext}(\vec{r})$; and, c) basis set generation for the description of KS linear atomic orbitals. These three approximations are discussed in detail in the following sub-sections.

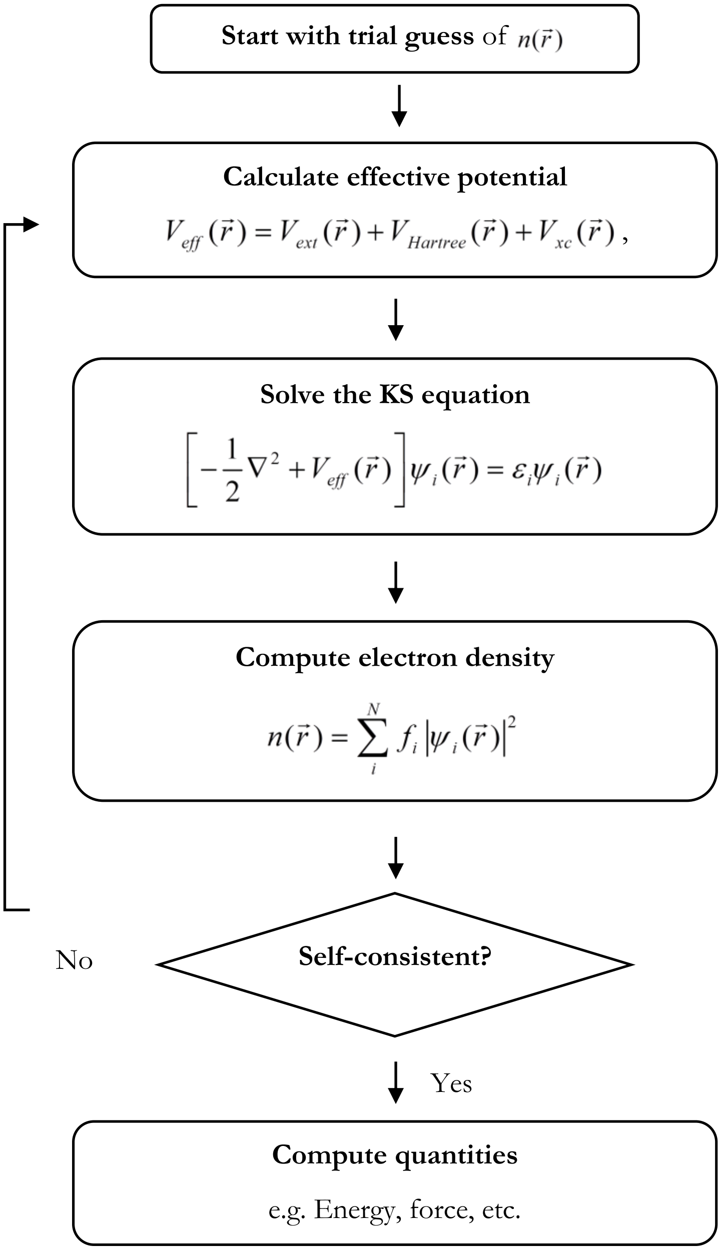

Figure 3.1: Schematic process of solving the self-consistent KS equation

3.2.3 Exchange-correlation (XC) functional

In the KS theorem, sophisticated many-body problems are transformed into a single particle problem. The XC functionals are critical for attempting to describe and include the many-body effects into DFT. There have been several formulations of XC to describe these effects, and the local density approximation (LDA) is the simplest and most commonly used in DFT. LDA is derived based on the fact that, in most of bulk solids, the electron densities are slowly varying; hence, the electrons can be described as homogeneous electron gas.

The common parameterization for LDA was first proposed by Perdew and Zunger (PZ) with including Monte Carlo (MC) correction.[50] Then Perdew and Wang (PW) developed this further by adding MC corrections for more materials.[51] The functional form of LDA is defined as:

$$E_{xc}^{LDA}[n(\vec{r})] = \int n(\vec{r})\varepsilon_{xc}(n(\vec{r}))dr \tag{3.9}$$

where ε_{xc} is the XC energy per the electron with the electron density, $n(\vec{r})$.

A modification of LDA, so-called local spin density approximation (LSDA), includes the spin effect of electrons.

In most of solid material cases, LSDA can reasonably identify material properties. However, it would fail to describe physics correctly when the electron density is non-homogeneous and varying fast (e.g. in molecules and atoms). To correct this, the generalized gradient approximation (GGA) is proposed. GGA contains the information for the gradient of the electron density, which provides better descriptions of the system, but makes computation more expensive. The functional form of GGA is defined as:

$$E_{xc}^{GGA}[n(\vec{r})] = \int n(\vec{r})\varepsilon_{xc}(n(\vec{r}), \nabla n(\vec{r}))dr \tag{3.10}$$

where ε_{xc} is the XC energy with the electron density, $n(\vec{r})$, and its gradient, $\nabla n(\vec{r})$.

The common functional forms for GGA were first derived by Perdew-Wang (PW91)[51]. Then PW91 was further improved by Perdew-Burke-Ernzerhof (PBE)[52] through adding corrections on the electron density gradient coefficients. After that, the PBE functional was verified and developed for specific materials and properties: RPBE (Revised Perdew-Burke-Ernzerhof) and PBEsol (PBE for solids). RPBE[53] improves assessments of the surface and atomization energies of molecules from PBE, while PBEsol[54] parametrization is specifically revised for solids and gives better lattice parameters than PBE.

In general, GGA provides more accurate results than LDA or LSDA. For example, GGA can reduce error in the total energy calculation and the over-estimation of the binding energy. However, GGA does not always capture the properties of the materials correctly. For example, GGA usually underestimates the band gap of the semiconducting materials, and provides too small adsorption energy of the molecules on the solid surface. Therefore, it is important to choose the correct parameterization of GGA for specific systems and the calculation of their properties. Towards more accurate results, a hybrid functional, which modifies the fraction of GGA exchange functions with more exact terms using Hartree-Fock method, was developed and first proposed by Becke.[55]

3.2.4 Pseudopotential[56]

In current theoretical understanding, core electrons do not contribute significantly to the description of the chemical bonding or the calculations of the other physical properties. In other words, they are chemically inert and highly localized around the nuclei. Furthermore, determining the wavefunction description of core electrons requires large computational costs because it needs a lot of basis set generations, unlike valence electrons. Therefore, the KS equation can be further simplified without losing much accuracy by including an estimation of their potential effects.

When generating the pseudopotentials, the following conditions must be satisfied:[56]

(a) The Pseudo valence wavefunctions agree well with the all-electron wave functions calculation beyond a chosen cutoff radius (R_c) of the core electrons.

(b) The norm of the pseudo wavefunctions has to be identical with that of the all-electron functions inside the core radius (R_c).

(c) The eigenvalues of pseudopotential functional have to be consistent with all-electron calculations.

It should be noted that the description of pseudopotentials is not always unique. By changing the cutoff radius (R_c), one can generate softer pseudopotential with larger Rc. This is less accurate and less transferable, because there are more unmatched wavefunctions inside Rc. However, by decreasing Rc, more transferability can be included in the potential description and can be applied to more complicated environments.

3.2.5 Basis set[3]

The KS equation can be solved by several numerical approaches, and introducing the basis set is one of the typical ways to solve the eigenvalue problem. It is important to choose an appropriate basis set, because this significantly affects the accuracy of the overall DFT energy calculation. There are two common methods of applying basis sets: the plane wave (PW) method and the localized orbital method. In the PW method, the accuracy of the calculation can be systematically improved by increasing the large number of waves. However, it requires very expensive computational resource to describe the real wavefunctions around the localized states (nuclei). On the other hand, one can solve the KS equation by projecting the atomic orbitals onto a linear combination of localized numerical atomic orbitals (LCAO). This method can still describe the periodic system as the PW method does, and it scales much better with more computational resource than PW method.

The accuracy of the localized orbital basis set generation is highly dependent on the basis size and shape. The number of basis set functions can be increased, adding more radial function using multiple-ζ basis set (e.g. dougle-ζ or DZ). In addition, a polarization effect can be introduced to include the angular flexibilization. For example, a Silicon atom (valance configuration of 3s^2, 3p^2) can be described using 13 basis sets applying DZP (double-ζ with polarization) setup. (i.e. 8 are from the radial functions and 5 are from the polarization function.) It is important to note that the DZP basis set is fairly accurate comparing to an even higher basis.[3] The energy of the system is improved significantly from SZ (single-ζ) to DZP, and it is almost even with the higher basis set (TZP, TZDP, and so on.)

To include the basis set in the KS theorem, the wavefunctions can be defined as:

$$\psi_i(\vec{r}) = \sum_{\alpha}^{M} c_{i\alpha}\phi_\alpha(\vec{r}) \tag{3.10}$$

where $c_{i\alpha}$ represents the weights of the contributions of the M atomic orbitals to the molecular orbital with α denoting the basis orbitals, and $\phi_\alpha(\vec{r})$ the basis function.

Now, the KS equation (Eq. (3.6)) can be replaced with Eq. (3.10), and it becomes

$$\sum_{\alpha}^{M} c_{i\alpha}\left[-\frac{1}{2}\nabla^2 + V_{eff}(\vec{r})\right]\phi_\alpha(\vec{r}) = \sum_{\alpha}^{M} c_{i\alpha}\varepsilon_i\phi_\alpha(\vec{r}) \tag{3.11}$$

Then the conjugate of the basis function, $\phi_{\beta}^{*}(\vec{r})$, can be multiplied and the equation can be integrated over all real space as:

$$\sum_{\alpha}^{M} c_{i\alpha} \int \phi_{\beta}^{*}(\vec{r}) \left[-\frac{1}{2}\nabla^{2} + V_{eff}(\vec{r}) \right] \phi_{\alpha}(\vec{r}) dr = \sum_{\alpha}^{M} c_{i\alpha} \varepsilon_{i} \int \phi_{\beta}^{*}(\vec{r}) \phi_{\alpha}(\vec{r}) dr \tag{3.12}$$

where $\int \phi_{\beta}^{*}(\vec{r}) \left[-\frac{1}{2}\nabla^{2} + V_{eff}(\vec{r}) \right] \phi_{\alpha}(\vec{r}) dr$ is the Hamiltonian (H) matrices and $\int \phi_{\beta}^{*}(\vec{r}) \phi_{\alpha}(\vec{r}) dr$ is the overlap (S) matrices. Then the final form of KS equation turns into the so-called "secular equation," which is given as:

$$\mathrm{H}C = \varepsilon SC \tag{3.13}$$

where C is the coefficient of basis sets and ε is the eigenvalues. Now, the secular equation of the KS equation becomes the generalized linear eigenvalue problem in matrix form, and it can be solved using standard mathematical libraries thus:

$$\sum (\mathrm{H} - \varepsilon S) C = 0 \tag{3.14}$$

3.3. Simulation Setup

To understand the physical and mechanical nature of C60 filled with water, DFT calculations using SIESTA were performed.[3] DFT is widely used because it can accurately capture the mechanical and electronic properties of nano-materials under various conditions.[57-61] For parameterization of the exchange-correlation functional, generalized gradient approximation (GGA) with revised Perdew-Burke-Ernzerhof (RPBE) is used.[52, 53] The core electrons are replaced by the norm-conserving pseudo-potentials.[62] For the basis set, double zeta basis plus polarization

(DZP) numerical atomic orbital is used. For the k-point mesh generation, the Γ point is used. To remove any artificial effect of interaction between $H_2O(n)@C60$ in the periodic simulation box, a vacuum region of around 15 Å is used in all directions. Structural relaxation is achieved until the maximum residual force of the system is reached, which is less than 0.03 eV/Å .

First, mechanical properties under hydrostatic strain are investigated. Hydrostatic pressure (P), and bulk modulus (B) are defined as $P = |dE / dV|$, and $B = V_0(\partial^2 E / \partial V^2)$, where E is the total energy and V is the volume of $H_2O(n)@C60$. The hydrostatic (volumetric) strain (ε_v) is defined as $\varepsilon_v = (V_s - V_0) / V_0$, where V_0 is the initial volume and V_s is the deformed volume. The hydrostatic strain is applied as follows: (a) The structure is relaxed for calculation of the initial total energy of the system. (b) Either tensile or compressive hydrostatic strain is applied to $H_2O(n)@C60$. (c) The strained C60 atoms are fixed and water molecules inside C60 are relaxed. (d) The total energy of the deformed system is computed. (e) Steps (b)-(d) are repeated until fracture of the system.

Mechanical properties under point load are also considered, and similar procedure, as introduced above, is used. Elastic modulus (E_p) and stress (σ) are defined as $E_p = (1/V_0)(\partial^2 U / \partial \varepsilon^2)$, and $\sigma = \partial U / \partial \varepsilon$; these are obtained from the variation of the strain energy (U) with applied strain (ε), which is defined as $\varepsilon = (d_s - d_0) / d_0$, where d_0 is the initial distance of two outermost carbon atoms in $H_2O(n)@C60$, d_s is the distance of two outermost carbon atoms when the strain is applied. Strain energy (U) is defined as E_s - E_0, where E_s is the total energy of the deformed system and E_0 is the total energy of the undeformed system. Point load is applied to $H_2O(n)@C60$ as follows: (a) The structure is relaxed for calculation of the initial total energy of the system. (b) Tensile or compressive strain is applied on two outermost carbon atoms on H_2O(n)@C60. (c) The two strained atoms are fixed, and other C60 atoms and water molecules inside C60 are relaxed. (d) The strain energy of the deformed system is computed. (e) Steps (b)-(d) are repeated until fracture of the system. Valentini *et al.* applied compression on silicon (Si) nanosphere using plates attached at both ends and showed that the applied load is distributed on the surface of ball. [63] We also performed MD simulations to apply compression using two plates and compared them with the current DFT result obtained using point load (see Supplementary Information).[64]

3.4. Results and Discussions

3.4.1. Structural properties of H_2O(n)@C60

Since water molecules can have different orientations inside C60, several structural relaxations with randomly oriented water molecules are performed to find energy-minimized structures, and they are used for mechanical deformations. The structural properties of each of the minimized H_2O(n)@C60 structures, such as C-C bond-length, interaction energy, and internal pressure are shown in Table 3.1. The initial C-C bond-length for C60 shows reasonable agreement with previous results.[65, 66] It should be noted that C-C bond-length increases as more water molecules are encapsulated due to the increase of interaction energy between water and C60. The interaction energy between water and C60 is computed as $E_{Interaction}=E_{H2O(n)@C60} - (E_{H2O(n)} + E_{C60})$, and the values from the initially relaxed structures are reasonable when compared to published results.[64] This expansion of buckyball can be also explained by the internal pressure increase which is induced due to encapsulation of water inside buckyball. In a related study, Pupysheva *et al.* showed that the bond-length of C60 can be increased as more hydrogen is filled.[39]

DFT and MD simulations were performed to calculate the internal pressure as shown in Table 3.1. MD simulation is only used for comparing the internal pressure with DFT. The internal pressure ($P_{I,\,DFT}$) using DFT is computed as $P_{I,\,DFT} = \left\langle \sum_{i=1}^{60} (F_i \cdot R_i) \right\rangle / (4\pi R^3)$, where F_i is the force vector on the ith carbon atom, R_i is the radius vector from the center of the buckyball, and R is the radius of the buckyball.[39]

To compute the pressure using MD simulation, we used LAMMPS package.[34] We used the energy minimized structure of C60 taken from DFT. Nosé-Hoover thermostat is applied to keep the temperature of H_2O(n)@C60 constant at 300 K. The simulation time step is chosen to be 0.1 fs. We employed the force field discussed in previous work.[67] Each simulation was run for 20 ns. Then the internal pressure ($P_{I,\,MD}$) is calculated as $P_{I,\,MD} = (Nk_BT)/V - (1/3V)\left\langle \sum_i \sum_{i>j} r_{ij}.F_{ij} \right\rangle$, where, N is the number of atoms, k_B is the Boltzmann constant, T is the temperature, V is the volume of C60, r_{ij} and F_{ij} are the distance and force between atoms i and j in the system, respectively. Both results confirm that adding more water molecules increase the internal pressure as shown in Table 3.1.

3.4.2. Mechanical properties under hydrostatic strain

First, we applied hydrostatic strain on $H_2O(n)@C60$ with tension and compression. The bulk modulus (Figure 3.2(a)) is obtained from the total energy variation with respect to the applied hydrostatic strain. The small strain region (-0.08 to 0.08 hydrostatic strain) is fitted using a 5th order polynomial. The bulk modulus of C60 is determined to be 742 GPa, and this is in reasonable agreement with the previous results.[43, 44] The bulk modulus increases with the number of water molecules in C60, but the enhancement is not significant.

The variation of the strain energy with the applied volumetric strain for different number of water molecules in C60 is shown in Figure 3.3(a). In general, all structures show similar energy variation for both types of loading. The effect of adding water molecules in C60 on the fracture behavior is clearly seen in Figure 3.3. For hydrostatic tension (HT), both the hydrostatic pressure and hydrostatic strain at fracture of $H_2O(n)@C60$ structure decrease as more water molecules are added as shown in Figure 3.3(c) and 3.3(d). Since the internal pressure and interaction energy are initially larger for structures with more water, less hydrostatic pressure is required to attain fracture under HT. Failure is initiated when the C-C bond is elongated up to around 1.85 Å.

Under hydrostatic compression (HC), it should be noted that the structure can withstand more than ~60 times the pressure at fracture than under HT. Unlike the tension case, the hydrostatic pressure and strain at fracture under compression increase for the 1 water case, but for 3 and 4 waters, they decrease slightly. This is because when the structure is highly compressed up to around fracture, the interaction energy between C60 and water is significantly increased, inducing the structural instability (e.g. at a compressive strain of 0.70, the interaction energy is 3.38 eV for 1 water, 55.16 eV for 3 waters, and 88.41 eV for 4 waters). This result indicates that the mechanical properties of water-filled (1-water) buckyball can be enhanced, but adding more water does not improve the fracture properties. In addition, it is interesting to note that at the same strain, the structure with more water molecules exhibits higher hydrostatic pressure. This means that one needs to apply more hydrostatic pressure to deform the more water-filled structure up to the same strain. Unlike the tension case, C-C bond dissociation is not observed for HC. In other words, failure of the structure under HC is initiated due to (a) the increased coordination number (from 3 to 5) of the carbon atom, and (b) the interaction between water molecules and $H_2O(n)@C60$ wall.

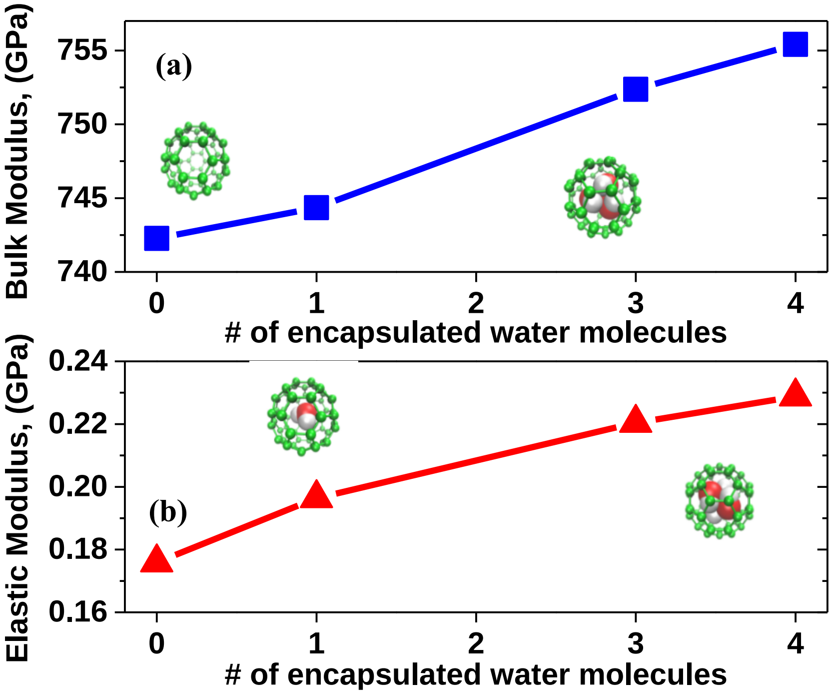

Figure 3.2: DFT results for mechanical properties of $H_2O(n)@C60$ structures, (a) bulk modulus vs. the number of encapsulated water, and (b) elastic modulus vs. the number of encapsulated water.

Structure	C-C Bond-length (Å) (Double, Single)	Total Energy (eV)	Interaction Energy (kcal/mol)	Internal Pressure (GPa)	
				DFT	MD
C60	1.407, 1.456	-9278.08	n/a	n/a	n/a
$H_2O(1)@C60$	1.411, 1.457	-9745.77	-17.34	0.01782	0.0049 (± 0.0012)
$H_2O(3)@C60$	1.418, 1.466	-10675.85	56.34	12.9883	3.97(± 0.45)
$H_2O(4)@C60$	1.424, 1.473	-11138.60	128.09	22.5763	27.45(± 1.345)

TABLE 3.1: DFT results for (2nd column) average C-C bond-length (double and single bonds), (3rd column) total energy of the initially relaxed system, (4th column) interaction energy between water molecules and C60. (5th column) DFT and (6th column) MD results for internal pressure due to water molecules.

3.4.3. Mechanical properties under point load

For the point load case, both tension and compression are applied to $H_2O(n)@C60$ structures. The mechanical properties are obtained from the strain energy variation with respect to the applied strain as shown in Figure 3.4(a). First, elastic modulus (Figure 3.2(b)) is computed using the small strain region (-0.03 to 0.03 strain) by fitting a 5th order polynomial. As more water molecules are introduced, the elastic modulus increases from 0.18 GPa to 0.23 GPa. The increase is not significant beyond three water molecules in C60.

Under the tensile point load, fracture stress and fracture strain decrease with the increase in the number of water molecules (Figure 3.4(c) and 3.4(d)). This behavior is similar to the HT case, which also can be explained by the increased interaction energy (Table 3.1) when more water molecules are added. The fracture of $H_2O(n)@C60$ is initiated due to the bond-breaking of the C-C bond from regions where the point load is applied. On the other hand, under the compressive point load, the structures with more water can withstand more stress with less fracture strain as shown in Figure 3.4(c) and 3.4(d), which is similar to the case of HC. The applied point load needs to overcome the increased interaction energy when compressed. When $H_2O(n)@C60$ is compressed, fracture stresses are comparable (0 and 1-water) or slightly larger (3 and 4-water) than those under tension. When the C60 wall is compressed and becomes closer to the water, carbon and oxygen atoms start to form a covalent bond which induces the structural instability, and bond dissociation is initiated at the wall after further deformation.

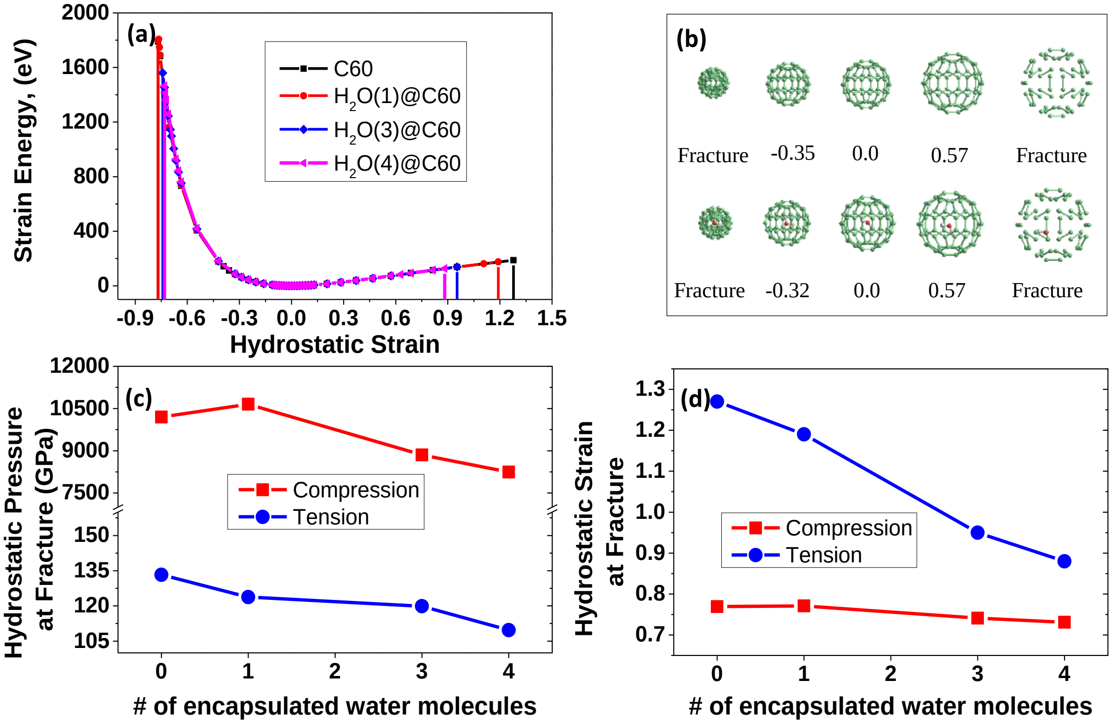

Figure 3.3: DFT results for (a) Strain energy vs. hydrostatic strain for $H_2O(n)@C60$ under hydrostatic compression (negative strain) and tension (positive strain). (b) Molecular structures (C60 (top row) and $H_2O(1)@C60$ (bottom row)) at each strain. (c) Hydrostatic pressure at fracture and (d) hydrostatic strain at fracture vs. the number of encapsulated water molecules under hydrostatic compression and tension.

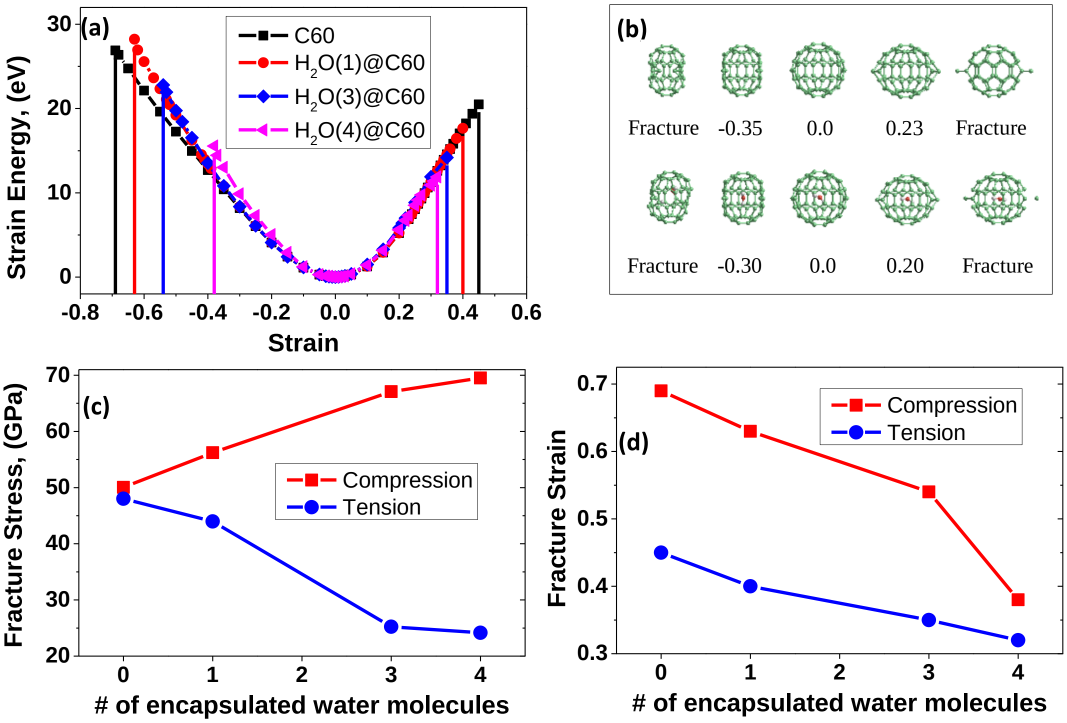

Figure 3.4: DFT results for (a) Strain energy vs. strain for $H_2O(n)@C60$ under compressive (negative strain) and tensile (positive strain) point load. (b) Molecular structures (C60 (top row) and $H_2O(1)@C60$ (bottom row)) at each strain. (c) Fracture stress and (d) fracture strain vs. the number of encapsulated water molecules under compressive and tensile point load.

Several interesting observations can be made for $H_2O(1)@C60$ structure. It has been shown that a single water molecule can rotate freely, meaning that there is no preferable orientation of water.[41, 42] Therefore, several tests are performed to verify that mechanical properties are not dependent on the water orientation. For the compression case, the plane of a water molecule is initially placed either perpendicular, horizontal or at a random orientation to the point load direction. It turns out that in all cases, the plane of the water molecule is positioned perpendicular to the loading direction after about 0.5 compressive strain, and it doesn't rotate further at a higher strain. In addition, strain energy variations for all the cases are the same. This result confirms that compressive response is independent of the orientation of water. For the fracture behavior, since a water molecule is in the middle of C60 due to the confinement effect, a covalent bond is formed between oxygen and carbon for a strain of 0.6 (bond-length of 1.384 Å, bond-energy of 6.0 eV). The hydrogen in water also forms a bond with the carbon atom (bond-length of 1.032 Å, bond energy of 5.3 eV). However, under tension, a water molecule stays where it was placed with no reorientation because carbon atoms are pulled away from a water molecule, so that the interaction between them is much weaker than in the compression case. For $H_2O(3, 4)@C60$ structures, under compression, the bond between carbon and water is formed around a strain of 0.53 (for 3 waters) and a strain of 0.37 (for 4 waters), which is smaller than in the single water molecule case. This bond formation leads to the failure of the system when further deformation is applied since it induces the structural instability of C60.

3.5. Conclusion

In this study, we investigated the effect of encapsulated water molecules inside C60 on its mechanical properties using DFT calculations. The hydrostatic strain and point load conditions are considered under both tension and compression. The effect of water molecules on the mechanical behavior of C60 is clearly observed in all cases. Under tension, both loading conditions show that the hydrostatic pressure at fracture and fracture stress decrease as more water molecules are added. Under compression, in contrast, structures can withstand more pressure (and stress) at the same strain with more water. This is because as more water molecules are added in C60, internal pressure and interaction energy between water and C60 increases. Fracture is initiated due to the bond formation between carbon and oxygen atoms under compression and bond-dissociation of carbon under tension. The study performed here suggests that water filled C60s can be good composite agents. Moreover, these results open up new idea that encapsulated molecules such as N_2, CO_2, etc, can potentially affect mechanical properties of C60 significantly under various loading conditions. Then these materials can be inserted into polymer materials to enhance the mechanical properties. In addition, mechanical modulation of endohedral C60s can be used to form new chemical compounds because under deformation, the nature of interaction between molecules and carbon can be significantly affected.

CHAPTER 4

MECHANICALLY-MODULATED ELECTRONIC PROPERTIES OF WATER-FILLED FULLERENES

4.1. Introduction

The encapsulation of a single water molecule, nitrogen, hydrogen, and other molecules/atoms in a C60 opens up new opportunities for designing new nano-scale devices.[7, 39, 40] The endohedral fullerenes have different structural and mechanical properties compared to empty fullerenes. Pupysheva *et al.* showed that a buckyball can be used for storage of multiple hydrogen molecules.[39] Shen studied the effect of having Si and Ge inside C60 on the mechanical response under compression.[48] In our previous study, we have investigated the mechanical properties of water-filled C60. [68] It has recently been shown that the rotational diffusion and entropy of a single water molecule inside C60 is an order of magnitude higher compared to the bulk molecule.[69]

The electronic properties of C60 can be highly affected from the interaction with molecules. Rivelino *et al.* studied C60 and hydrated C60 using Monte Carlo/DFT and showed that the electronic properties (specifically, energy gap) change due to the interaction between C60 and outside water molecules.[70] Kawahara *et al.* showed that the Density of States (DOS) of C60 can be significantly modified when deposited on Cr(001) surface.[71] It is noteworthy that mechanical deformation can also significantly affect the electronic properties of nano-materials. In a relevant study, Ni *et al.* showed that the uniaxial tension of graphene can open a band gap of about 300 meV.[72] Similar study was done by Yang *et al.* for carbon nanotubes (CNT), and they demonstrated that the uniaxial and torsional deformation can modify the band gap of CNT. [73] Mechanically induced electronic changes in nano structures can enable the design of novel electronic devices such as bio-sensors and field effect transistors (FETs).[72-74] Scalise *et al.* showed that the semiconducting to metallic transition of MoS_2 occurs when a compressive or tensile deformation is applied. [74] The effect of mechanical stimuli on the electronic properties of fullerenes and water-filled fullerenes' is still unknown and understanding these effects can enable new applications such as molecular sensing devices.

In this study, we present the effect of mechanical deformation on the electronic structure of empty and water-filled fullerenes ($H_2O(n)@C60$, $H_2O(10)@C180$, and $H_2O(18)@C240$, where n is the number of water molecules inside the fullerenes). We first filled fullerenes with water molecules using molecular dynamic simulations (MD), and then exported the geometries for quantum simulations using the density functional theory (DFT). A point load is applied for mechanical deformation tests by considering both tension and compression. The change in energy gap of all structures with respect to the applied strain is studied.

4.2. Methods and Simulation Setup

DFT calculations were performed using the SIESTA package on empty and water-filled fullerenes to understand the change in structural and electronic properties under mechanical deformation.[3] DFT calculations have been shown to be accurate for mechanical and electronic properties of nano-materials under various conditions.[57-61, 68, 70, 71, 75] For parameterization of the exchange-correlation functional, generalized gradient approximations (GGA) with revised Perdew-Burke-Ernzerhof (RPBE) is employed.[52, 53] The core electrons are replaced by the norm-conserving pseudo-potentials.[62] For the basis set generation, double zeta basis plus polarization (DZP) numerical atomic orbital is used, and the Γ point is applied for the k-point mesh generation. To remove any artificial effect of interaction between structures in the periodic simulation box, a vacuum region of around 15 Å is used in all directions. Structural relaxation is performed until the maximum residual force of the system is less than 0.03 eV/Å .

To understand the electron clouds overlap/charge transfer due to the interaction between water and fullerene, the charge density rearrangement ($\Delta\rho$) is obtained, which is defined as $\Delta\rho = \rho_{Fullerene+Water} - (\rho_{Fullerene} + \rho_{Water})$, where $\rho_{Fullerene}$ and ρ_{Water} represent the charge density distribution of each isolated structure (fullerene and water), and $\rho_{Fullerene+Water}$ is the charge density distribution of the total system. The interaction energy between water molecules and fullerene, shown in Table 4.1, is calculated as $E_{Interaction} = E_{Total} - (E_{H_2O(n)} + E_{Fullerene})$, where $E_{H_2O(n)}$ and $E_{Fullerene}$ are the energies of isolated water and fullerene (C60, C180, and C240), respectively, and E_{Total} is the energy of the total system.

The change in energy gap of water-filled fullerenes under a point load is obtained using the following procedure. (a) The structure is relaxed for calculation of the initial energy gap, which is defined as the energy difference between the highest occupied molecular orbital (HOMO) and the lowest unoccupied molecular orbital (LUMO) of the system. (b) Tensile or compressive point load is applied on the two outermost carbon atoms of fullerenes in the x-direction. The applied strain (ε) is defined as $\varepsilon = (d_s - d_0) / d_0$, where d_0 is the initial distance of the two outermost carbon atoms in the fullerene, and d_s is the distance of the two outermost carbon atoms when the strain is applied. (c) The two strained atoms are fixed while other fullerene carbon atoms and water molecules inside the fullerene are relaxed. (d) The energy gap of the deformed structure is obtained. (e) Steps (b)-(d) are repeated for each system (empty vs. water-filled structures) to determine the energy gap. Valentini *et al.* used plates at both ends to apply compression on a nanosphere, and showed the load distribution on the surface of the nanosphere.[63] As discussed in the previous study[68], using the point load method performed here is a reasonable approach to apply tension and compression on the fullerenes.

Each fullerene structure is initially filled with water molecules using MD simulations. The number of equilibrated water molecules inside C60, C180, and C240 are 1, 10, and 18, respectively. For C60, a higher number of water molecules (3 and 4 water) is also studied. In MD simulations, first, for each fullerene, 11-15 carbon atoms were removed from the structure. Then, the holed fullerene structure was inserted in a bath of water molecules (a water box of 8 nm × 8 nm × 8 nm was used). SPC/E water model was used. The fullerene structures were then minimized using NPT simulation for 2 ns. For all the structures, complete water-filling occurred in less than 500 ps. After water-filling was observed, the simulation was continued and the average number of water molecules in each structure was calculated. The fullerene structure with the average number of water molecules was selected, and the atomic coordinates were imported into DFT. Then the structures were further relaxed in DFT before applying deformation.

Structure	C-C Bond-length (Å)	Interaction energy (kcal/mol)	Energy gap (eV)
C60	1.4315	n/a	1.65
$H_2O(1)@C60$	1.4340	-17.34	1.62
$H_2O(3)@C60$	1.4420	56.34	1.48
$H_2O(4)@C60$	1.4485	128.09	1.27
C180	1.4346	n/a	1.44
$H_2O(10)@C180$	1.4359	-67.33	1.39
C240	1.4337	n/a	1.22
$H_2O(18)@C240$	1.4343	-102.75	1.19

TABLE 4.1: The effect of water encapsulation inside fullerenes (C60, C180, and C240) on structural and electronic properties. (2nd column) Initial average bond-length of carbon-carbon, (3rd column) interaction energy between water and fullerene, (4th column) the initial energy gap of all systems. The bond-length and interaction energy for $H_2O(n)@C60$ are taken from the previous work.[68]

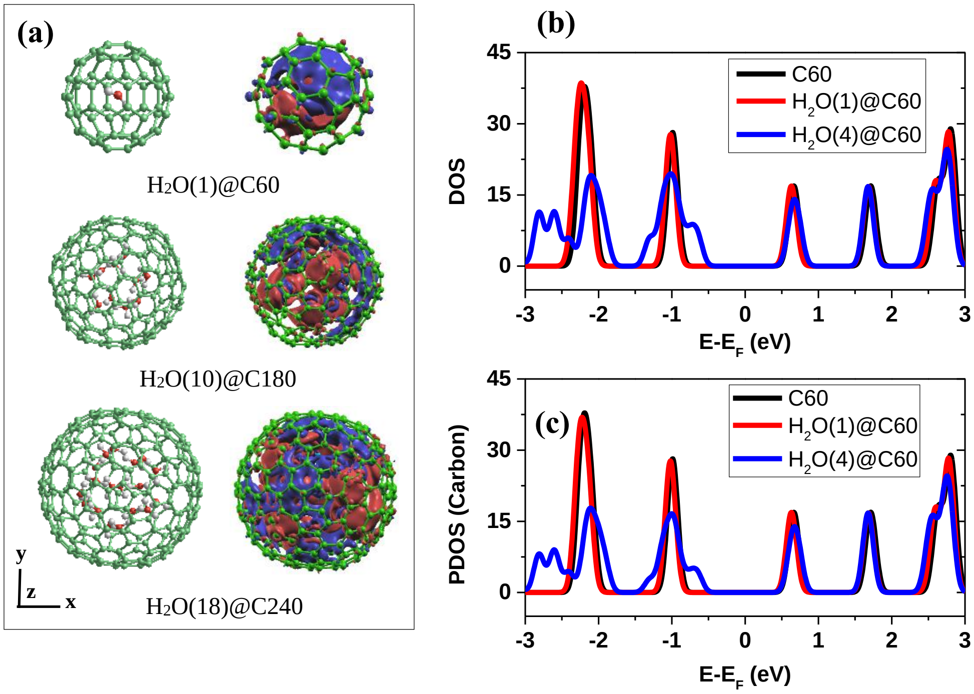

Figure 4.1: (a) (Left) Molecular structures and (Right) 3D charge density rearrangement ($\Delta\rho$) of water-filled fullerenes. (Red and blue isosurface represent charge accumulation and depletion, respectively. Isosurface level is set at 0.0003 Å^{-3}.) (b) Density of States (DOS), and (c) Partial Density of States (PDOS) of C60 and $H_2O(n)$@C60, where n=1, 4.

4.3. Results and Discussions

4.3.1 Structural and electronic properties of fullerenes

Three different types of fullerenes - $H_2O(n)@C60$, $H_2O(10)@C180$, and $H_2O(18)@C240$ are considered in this study. The schematic of these structures is shown in Figure 4.1(a). When water molecules are encapsulated inside the fullerenes, there is a clear rearrangement of the charge density ($\Delta\rho$) due to the interaction between water and fullerene (Figure 4.1(a)). It can be inferred from Figure 4.1(a) that there is an exchange/overlap of electrons in the system due to water encapsulation.

We first computed the initial bond-length for all empty fullerenes of C60, C180 and C240 (all three structures are around 1.43 Å, shown in Table 4.1) and they are in reasonable agreement with previous studies (around 1.41 Å to 1.44 Å).[66, 70, 76, 77] The bond-length of fullerenes is elongated when water molecules are inside, but the increase is not significant. The interaction energy calculations (shown in Table 4.1) for $H_2O(1)@C60$, $H_2O(10)@C180$, and $H_2O(18)@C240$ confirm that water molecules can be naturally encapsulated in the fullerene. The interaction energy becomes positive if more water molecules are encapsulated as observed for 3 and 4-waters in C60. The energy gap of naturally water-filled structures is slightly lower compared to the empty ones as shown in Table 4.1. In addition, the energy gap decreases as the size of the fullerene increases. It can also be inferred from Table 4.1 that introducing more waters (3 and 4 water molecules in C60) can further affect the fullerene structures and decrease the energy gap. Density of States (DOS) for the total system (water + fullerene) and Partial Density of States (PDOS) for the fullerene in the total system are shown in Figure 4.1(b) and 4.1(c). They confirm that when more water is added, there are new energy states introduced around -0.8 eV for $H_2O(4)@C60$ compared to C60. As a result, the energy gap of $H_2O(4)@C60$ is further reduced compared to the empty C60.

4.3.2 Energy gap of $H_2O(n)@C60$ under a point load

First, we applied a compressive point load on an empty C60, and computed the energy gap for each applied strain (Figure 4.2(a)). As the applied strain increases, the energy gap first decreases. It should be noted that after around -0.4 strain, the energy gap starts to increase slightly and drops around the fracture point. Interestingly, when one water molecule is encapsulated ($H_2O(1)@C60$), we observe a different response on the energy gap variation. It should be noted that the initial water orientation effect is not considered in this study because previously, we showed that the orientation of water molecules does not play a significant role under an applied compression load.[68] Unlike in the empty C60, the energy gap of $H_2O(1)@C60$ decreases with the increase in strain. To further verify the effect of water encapsulation, the same mechanical tests are performed on $H_2O(3)@C60$ and $H_2O(4)@C60$, and the same response as in $H_2O(1)@C60$ is observed. We also performed the tensile test, but the change in the energy gap for all the structures is similar to each other, i.e. the energy gap decreases with the increase in strain. No water encapsulation effect is observed for the tension case. This means that under compression, the increased interaction between water and the fullerenes plays a significant role in the variation of the energy gap.

The change in the energy gap observed under compression can be explained by the interaction energy, and the atomic bond distance between water and carbon atoms in $H_2O(n)@C60$ during deformation. For $H_2O(1)@C60$ and $H_2O(3)@C60$ structures under compression, the interaction energy is almost the same as its initial value up to around -0.35 strain, but increases

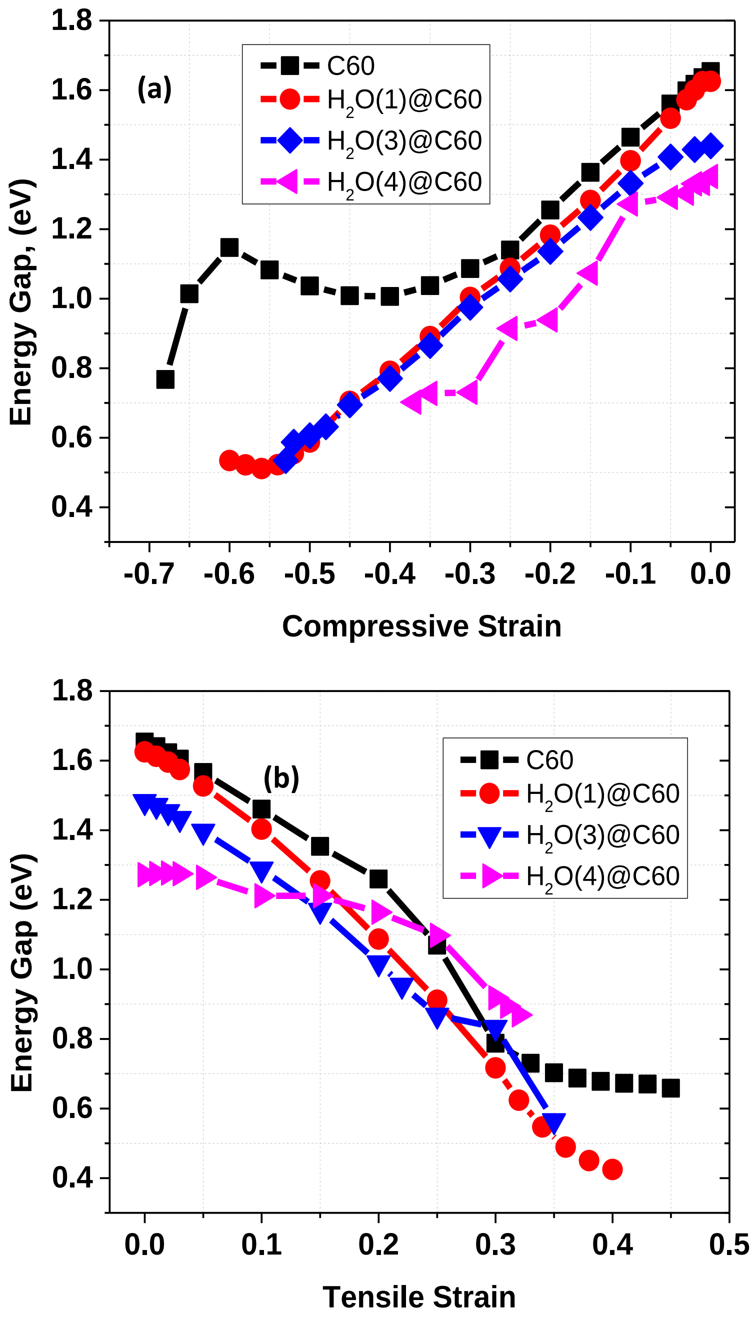

Figure 4.2: Energy gap as a function of strain for C60 and $H_2O(n)@C60$ under (a) compressive strain, and (b) tensile strain

rapidly as the compressive (negative) strain is increased further (Figure 4.3(a)). This strain of around -0.35 is when the energy gap variation starts to deviate between empty and water-filledC60s (Figure 4.2(a)). The change in the interaction energy during deformation confirms that the decrease in the energy gap in $H_2O(n)@C60$ is due to the enhanced interaction between C60 and water molecules. The distance between carbon and oxygen atom in $H_2O(1)@C60$ is obtained to supportthe increased interaction between them (Figure 4.3(b)). As the compressive strain increases, carbon atoms come closer to the water molecule. After a compressive strain of about -0.4, an oxygen atom in water is strongly attracted to one (Carbon (B)) of the carbon atoms where the point load is applied, and this eventually leads to the formation of a covalent C-O bond around fracture strain.[68]

Under tension, on the other hand, the interaction energy stays almost the same as its initial value (Figure 4.3(a)). This explains why there is no characteristic change in the energy gap for water-filled C60 under tension, compared to empty C60. We calculated the induced strain in the transverse (y and z) directions due to the point load for $H_2O(1)@C60$. Transverse strain (ε_{trans}) is defined as $\varepsilon_{trans} = (d_{ts} - d_{to}) / d_{to}$, where d_{ts} is the diameter in the transverse direction for the deformed structure, and d_{to} is the diameter in the transverse direction for the undeformed structure. The calculated values for ε_{trans} are -0.018 and -0.017 in the y and z directions for a tensile strain of 0.15, and -0.030 and -0.026 in the y and z directions for a tensile strain of 0.30. This implies that under tension, the distance between water and carbon wall increases in the loading direction while it stays almost the same in the transverse direction. Therefore, the interaction energy is not affected significantly.

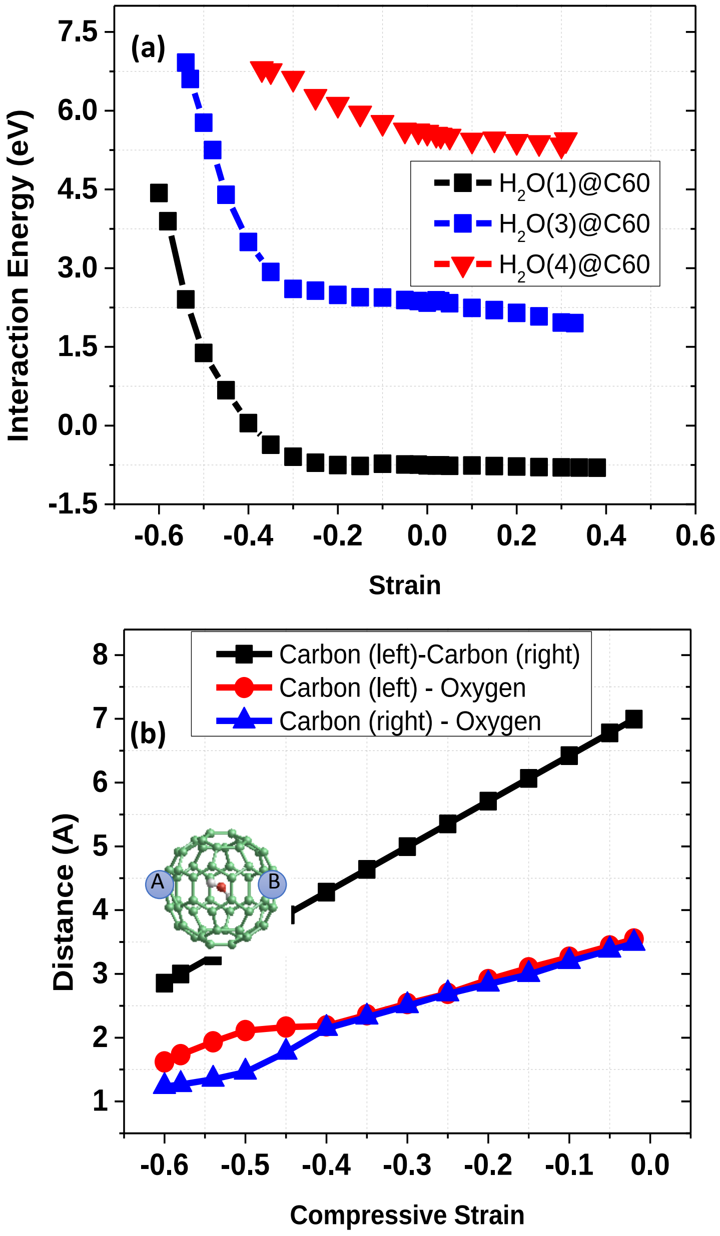

Figure 4.3: (a) Interaction energy between C60 and water for $H_2O(n)$@C60 under compressive (negative) and tensile (positive) strain. (b) Atomic distance of carbon-carbon and carbon-oxygen under compressive strain for $H_2O(1)$@C60. (Inset: Carbon atoms A and B represent atoms where the point load is applied.)

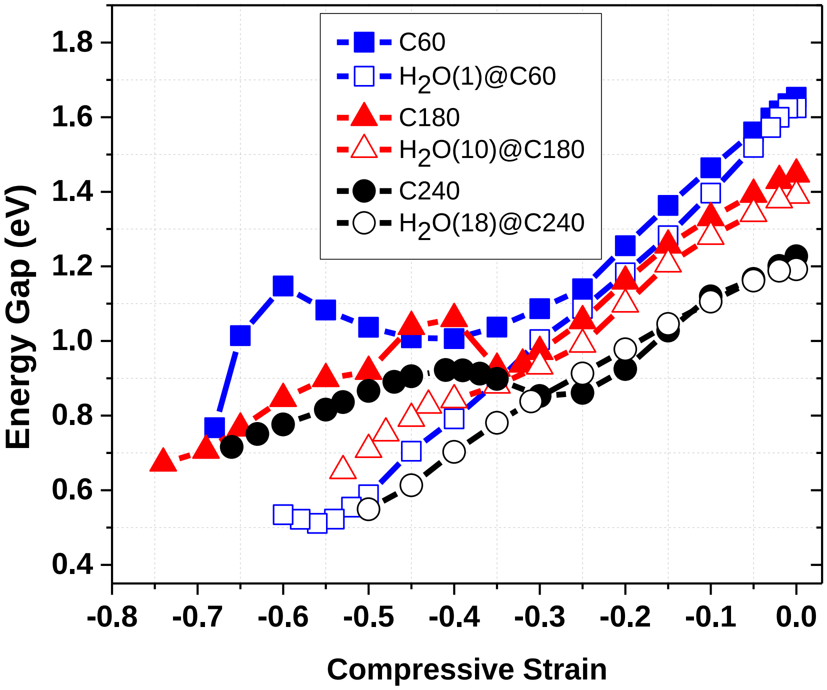

Figure 4.4: Energy gap as a function of compressive strain of empty and water-filled fullerenes (C60, C180 and C240).

4.3.3 Energy gap change of fullerenes ($H_2O(10)@C180$, $H_2O(18)@C240$) under a point load

We extended our work to investigate other endohedral fullerene structures such as $H_2O(10)@C180$ and $H_2O(18)@C240$. The compressive point load is applied to both empty and water-filled fullerenes, and the change in the energy gap with applied strain is obtained (Figure 4.4). Similar to C60 and $H_2O(n)@C60$ cases, there is a clear deviation in the variation of the energy gap between empty and water-filled structures during deformation. It is interesting to note that the threshold strain (the strain at which the energy gap of the endohedral structure deviates from the corresponding unfilled water structure) for all three fullerene structures (C60, C180 and C240), is around -0.35 ~ -0.40. These results can be used as a signature for differentiating between the empty and water-filled fullerenes.

4.4. Conclusion

In this study, we investigated the effect of encapsulated water molecules inside fullerenes ($H_2O(n)@C60$, $H_2O(n)@C180$, and $H_2O(n)@C240$) on the variation of energy gap under mechanical deformation using DFT calculations. The point load is applied using both tension and compression. The effect of encapsulated water molecules is clearly observed in all the structures under compression. A clear variation of the energy gap is observed for all the water-filled fullerenes, compared to the empty fullerenes, as the applied compressive strain increases. This is due to the increase in the interaction energy between water molecules and the strained carbon wall. Unlike compression, no clear effect of water on the energy gap is observed under tension. This is because of the weak interaction between the water molecules and the fullerene wall.

CHAPTER 5

BAND GAP MODULATION OF MOS_2 ON *a*-HFO_2

5.1. Introduction

A single-layer MoS_2, which is a semiconducting material with a direct band gap of 1.8 eV, has brought a lot of attention because it has been shown that the electron mobility of MoS_2 at room temperature is comparable to that of graphene nanoribbon.[2] Since then, there have been many attempts to investigate the mechanical,[78, 79] electronic properties,[80-82] and the sensing behaviors[83] of MoS_2 under various conditions as well as the band gap modulation with respect to the external mechanical deformation.[74, 84]

The deposition of electronic material on top of high dielectric (*k*) constant materials can significantly affect its electronic properties due to interaction between two structures. Providing information on modified material properties is critical. For example, the rippling of deposited structure can be induced due to interaction with the substrate and as a result, decreases the electron mobility of deposited material.[85] In addition, because of the electron overlap behavior between two structures, unique doping effect (*n*- or *p*-type doping) can be introduced.[85-88] In previous studies, Scopel *et al.* studied graphene adsorbed on amorphous HfO_2 structure, and demonstrated that HfO_2 can significantly perturb the surface potential of graphene.[85] Another well-known dielectric material, SiO_2, is also investigated when it interacts with MoS_2 by Dolui *et al.*[87] They examined the effect of impurities and defects in SiO_2 on the electronic properties of MoS_2 using first principle theory. They also have shown the origin of the doping effect in MoS_2, which is induced from Na impurities and oxygen dangling bonds in SiO_2 surface.

In this study, we investigate the electronic properties change of MoS_2 adsorbed on the top of amorphous HfO_2 (a-HfO_2). Amorphous structure of HfO_2 is considered to provide more realistic structural condition for interaction between MoS_2 and a-HfO_2 system. The band gap modulation, doping effect, effect of structural defects, and binding nature between two layers are investigated. In addition, the effect of electric field, which is applied in two different directions, on the band gap change is studied.

5.2. Methods and Simulation setup

We first generate a-HfO_2 structure using molecular dynamics (MD) simulations with LAMMPS package.[34] MD simulations are performed because they can generate and properly capture the amorphous structural properties.[89, 90] To describe the atomic interactions for hafnium (Hf) and oxygen (O) atom, charge optimized many body (COMB) potential is used. [91] We use the time step of 0.1 fs, and NPT is used with Nosé-hoover thermostat and barostat. Typical annealing and quenching process is applied to generate an amorphous structure of HfO_2. The monoclinic type of HfO_2 is first constructed and relaxed at 300 K, then the system temperature is increased to 4000 K and maintained. After annealing, the system is cooled down to 300 K, and maintained. For each step, 1 ns of the simulation time is used. After quenching process, the bulk density of a-HfO_2 at 300 K is determined to be 8.295 ± 0.03 g/cm^3, which shows good agreement with the previous results.[85, 92] After generating a-HfO_2 in MD simulations, the atomic coordinates are exported to density functional theory (DFT) scheme for further energy minimization.

To investigate the electronic properties change of MoS_2 adsorbed on a-HfO_2, we implemented DFT simulation with SIESTA package.[3] DFT is chosen because there have been several relevant studies which captured the electronic properties of nano-materials under various conditions.[57-61, 68, 81, 83, 85, 87] For parameterization of the exchange-correlation functional, generalized gradient approximation (GGA) with Perdew-Burke-Ernzerhof (PBE) is employed.[52] The core electrons are replaced by the norm-conserving pseudo-potentials.[62] For the basis set generation, double zeta basis plus polarization (DZP) numerical atomic orbital is used. For Monkhorst-Pack k-point generation, 6 x 6 x 1 for structural relaxation and 12 x 12 x 1 for electronic properties calculation are applied.[93] A vacuum regions of around 20 Å is used for z-direction in the periodic box to avoid unphysical effect. The structures are relaxed before obtaining the electronic properties until the maximum residual force of the system is less than 0.05 eV/Å.

To understand the modified electron density due to the interaction between MoS_2 and a-HfO_2, the charge density rearrangement ($\Delta\rho$) is obtained. It is defined as $\Delta\rho = \rho_{MoS_2+HfO_2} - (\rho_{MoS_2} + \rho_{HfO_2})$, where ρ_{MoS_2} and ρ_{HfO_2} represents the charge density distribution of each structure (MoS_2 and a-HfO_2), and $\rho_{MoS_2+HfO_2}$ is the charge density distribution of the total system (MoS_2 + a-HfO_2). The binding energy between MoS_2 and a-HfO_2 shown in Table I is calculated as $E_{Binding} = E_{MoS_2+HfO_2} - (E_{MoS_2} + E_{HfO_2})$, where E_{MoS_2} and E_{HfO_2} is the energy of MoS_2 and a-HfO_2, respectively, and $E_{MoS_2+HfO_2}$ is the energy of the total system (MoS_2 + a-HfO_2).

5.3. Results and discussions

5.3.1 Electronic and structural properties – MoS_2 and a-HfO_2

A single layer MoS_2 with 48 atoms is constructed as shown in Figure 5.1(a). After structural minimization, the bond-length of Mo-S (2.444 Å), S-S (3.193 Å) and lattice constant (a = 3.204 Å) are obtained, and they show good agreement with previous results.[80, 94] It has been confirmed by several experimental and simulation results that the single layer MoS_2 has a band gap of 1.6 eV ~ 2.1 eV.[2, 94, 95] In this study, the band gap (MoS_2, suspended) is obtained as 1.68 eV, which is comparable with previous results. For a-HfO_2, we obtained the electronic and fundamental structural properties. The electronic density of states (DOS) of a-HfO_2 showed that the band gap of a-HfO_2 is calculated as 3.58 eV (Figure 5.1(b)), which is comparable to the previous studies.[78, 92] To verify the amorphous structure of HfO_2, the coordination number for Hf and O is calculated. (Figure 5.1(c)) The number of bonds are counted when the bond-length is within 2.5 Å.[92] In addition, radial distribution function (RDF) is examined (Figure 5.1(d)), and the peak for Hf-Hf, Hf-O, and O-O are 2.15 ± 0.15 Å, 2.55 ± 0.13 Å, and 3.35 ± 0.18 Å, respectively. All calculated properties for a-HfO_2 showed good agreement with the previous reference.[92]

5.3.2 MoS_2 adsorbed on a-HfO_2

After verifying the initial structural and electronic properties of both structures, pristine MoS_2 is placed on the top of pristine a-HfO_2 and relaxed. First, there is no significant change in the structure of MoS_2 as shown in Figure 5.2(a), which indicates the interaction between two substrates is weak. Then we compared DOS of MoS_2-suspended and MoS_2- supported (Figure

5.2(b) and 5.2(c)). They show that there is no significant difference in the general shape of partial density of states (PDOS) for both cases. For the band gap of supported MoS_2, it is reduced by about 0.12 eV from its suspended structure, which becomes 1.58 eV. It should be noted that no doping effect has been observed for MoS_2- intrinsic semiconductor.

To identify the structural and electrostatic effect due to a-HfO_2 structure, we increase the interlayer distance between MoS_2 and a-HfO_2 manually by adding 1 Å, and 2 Å to its initially relaxed distance (1.906 Å). We also compared the band gap of MoS_2 (MoS_2, detached) by removing a-HfO_2 from the relaxed structures of MoS_2 + a-HfO_2. In Figure 5.2(d), it confirms that as both substrates are separated farther, the band gap is less affected. Binding energy calculation shows that it decreases from 2.96 eV (supported), 1.18 eV (+ 1 Å) to 0.11 eV (+ 2 Å) as the separation distance increases. When MoS_2 is finally detached from a-HfO_2, the band gap of MoS_2 is fully recovered to its original (MoS_2, suspended) value, 1.68 eV. This result indicates that there is only electrostatic interaction effect from a-HfO_2 on MoS_2, and the structure of MoS_2 is not deformed when adsorbed on a-HfO_2.

5.3.3 MoS_2 adsorbed on defective a-HfO_2

It should be noted that defective sites in a-HfO_2 can significantly affect and modify the electronic DOS for a-HfO_2 itself and its interacting material above. In a relevant study, it has shown that the oxygen vacancy (VO) in a-HfO_2 can induce *n*-type doping to adsorbed graphene.[85, 88] We introduced the same defective sites (VO) on a-HfO_2 and investigated its effect on MoS_2. First, the interlayer distance is decreased (1.906 to 1.692 Å, Table I) from the pristine case thus binding energy is increased. (2.96 to 6.94 eV Table I). Furthermore, the electron density rearrangement shown in Figure 5.3(a) and 5.3(b) confirms that when VO is introduced, there is more electron cloud overlap compared to the pristine a-HfO_2 case.

The total DOS in Figure 5.4(a) shows that band gap of MoS_2 + a-HfO_2 (VO) is further reduced to 1.4144 eV. In addition, MoS_2 becomes *n*-type doped semiconductor- PDOS of MoS_2 is shifted to the left comparing to its intrinsic case. To examine the source of *n*-doping characteristic, we detached MoS_2 from the relaxed MoS_2 + a-HfO_2 (VO) structures. When detached, PDOS of MoS_2 is shifted back to its initial location (neutral), which means that *n*-type behavior in MoS_2 is originated due to the presence of oxygen vacancy in a-HfO_2. In previous studies, the origin of *n*-type doping on graphene and MoS_2 is investigated, which is due to electron donor states from defective sites in a-HfO_2 or SiO_2.[85, 87, 88] PDOS of a-HfO_2 in Figure 5.4(a) also confirms that there are donor states introduced around -0.1 eV.

Regarding band gap change, it is interesting to note that the band gap of detached MoS_2 from the structure of MoS_2 + a-HfO_2 (VO) is 1.52 eV (Figure 5.4(b)), which is not fully recovered to its bulk value (1.69 eV). This result means that the structure of MoS_2 is deformed due to its stronger interaction with a-HfO_2 (VO). The electrostatic effect from a-HfO_2 on the band gap of MoS_2 is calculated (1.52 eV - 1.41 eV = 0.10 eV), and the structural deformation effect is calculated as (1.69 eV - 1.52 eV = 0.16 eV). To verify the effect of increased number of defects on a-HfO_2, the number of VO on a-HfO_2 is added. It shows that the band gap of MoS_2 is further reduced when more defects are introduced- 1.20 eV and 1.18 eV for 2-VO and 4-VO cases, respectively. When MoS_2 band gap is reduced interacting with pristine a-HfO_2 to a-HfO_2 (4VO) substrate, the interlayer distance is decreased from 1.90 Å to 1.57 Å, while the binding energy increases from 2.96 eV to 11.43 eV (Table 5.1).

5.3.4 Defective MoS_2 adsorbed on pristine and defective a-HfO_2

We also introduced the defects on MoS_2 and investigated their effect on the electronic structure. For MoS_2 structure, there could be two defective sites, Mo or S vacancy (VMo, VS). Since S atom is on the surface of MoS_2, two cases are considered, VS and VS + VMo. For the case of VS, it has been shown that VS can induce the localized finite states in the middle of band gap of a single layer MoS_2.[82] The similar behavior has also been observed in current study as shown in DOS (Figure 5.5(a)), and the band gap of MoS_2 (VS) is computed as 1.0012 eV. For MoS_2 (VS + VMo) case, MoS_2 becomes metallic as observed in Figure 5.5(b). It is interesting to note that introducing VS on MoS_2 does not increase its interaction with a-HfO_2. The interlayer distance and binding energy information for MoS_2 (VS) + a-HfO_2 in Table 5.1 show that they are almost comparable to those of MoS_2 + a-HfO_2 case. For the interaction of MoS_2 (VS) with a-HfO_2 (VO), the band gap is further reduced from 1.00 eV to 0.96 eV (Figure 5.5(c)). As similarly shown for MoS_2 + a-HfO_2 (VO), there are more clear charge accumulation and depletion regions for the structure of MoS_2 (VS) + a-HfO_2 (VO) as shown in Figure 5.3(c) and 5.3(d).

In summary, the band gap variation for all configurations is shown in Figure 5.6. For pristine MoS_2, introducing defects in a-HfO_2 decreases the band gap from 1.7 eV (suspended) to 1.4 eV- when interacting with defective a-HfO_2. The band gap can be further reduced by increasing the number of oxygen vacancies in a-HfO_2. For defective MoS_2 structures, interacting with a-HfO_2 (pristine or VO) does not significantly affect the band gap.

5.3.5 Effect of External Electric Field

Field effect transistors (FET) uses the vertical electric field (gate voltage) to control the channel conductivity of the semiconducting layer between source and drain.[96] In addition, applied electric field can significantly modulate the electronic structure of the system such as the band gap and the electron distribution in FET. In a previous study, it is shown that the transverse electric field can affect the band gap of armchair MoS_2.[97] For the bilayer structure of MoS_2, applying vertical electric field can decrease the band gap, and finally, the structure becomes metallic.[98] Similarly, the electric field can significantly affect the band gap of a single layer of MoS_2 when wrinkles are formed, which enlarge its dimension in the vertical direction.[99]

To fabricate FET using the structure of MoS_2 deposited on a-HfO_2, it is important to understand electrical properties change of MoS_2 under vertical electric field. Since a-HfO_2 substrate exhibits the large effect on the electronic structure of MoS_2, the interaction between two substrates is expected to be affected significantly under vertical electric field. The schematic view of how the electric field is applied to the substrates is shown in Figure 5.7(a). Electric field is applied to the system (MoS_2 + a-HfO_2) with respect to two different directions, i.e. from top to bottom (negative) and from bottom to top (positive).

We first obtain the band gap change of the whole system (MoS_2 + a-HfO_2) when electric field is applied (Figure 5.7(b)). As we increase the electric field in the top to bottom direction, the band gap is decreased immediately then finally becomes almost 0 eV at 0.7 V/Å . On the other hand, in the bottom to top direction, the band gap stays around its initial value at first, then starts to decrease significantly when applied electric field is beyond 0.3 V/Å .

When the external electric field is applied, the electrons in the system are redistributed. To understand this, we first calculate the carrying charge of each atom by obtaining the Mullliken charge distribution in MoS_2 + a-HfO_2 (pristine) system without the electric field.[100] For this structure, MoS_2 has 287.795 electrons in total, which is less than that of freestanding MoS_2, 288 electrons. This indicates when a-HfO_2 is pristine, MoS_2 is positively charged while a-HfO_2 is negatively charged.

The charge transfer between two substrates can be further supported by the PDOS change of MoS_2 and a-HfO_2 under different directions of the electric field (Figure 5.8). Increasing electric field in the negative direction can shift PDOS of MoS_2 to the left (*n*-type direction) while PDOS of a-HfO_2 moves to the right (*p*-type direction), as shown in Figure 5.8(a). This means that electrons are transferred from a-HfO_2 to MoS_2. Since MoS_2 is initially positively charged, after getting electrons from a-HfO_2, it is less positively charged while a-HfO_2 is less negatively charged. In addition, the instant decrease in band gap under negative electric field can be explained as follows. The band gap of MoS_2 + a-HfO_2 is computed from the lowest unoccupied molecular orbital (LUMO) of MoS_2 and the highest occupied molecular orbital (HOMO) of a-HfO_2 as previously shown in Figure 5.2(b). Therefore, as more electric field is applied, LUMO of MoS_2 and HOMO of a-HfO_2 comes closer; hence, the band gap decreases (see Figure 5.7(b) and Figure 5.8(a)).

Under positive electric field, the behavior of PDOS shift for each of MoS_2 and a-HfO_2 is observed to be in the reverse direction (Figure 5.8(b)). Since electrons are transferred from MoS_2 to a-HfO_2, PDOS of a-HfO_2 is shifted to the left (more negatively charged) while PDOS of MoS_2 is moved to the right (more positively charged) as a stronger positive electric field is applied. In addition, it should be noted that up to around 0.3 V/Å , the band gap of MoS_2 + a-HfO_2 stays almost the same as its initial value. This is because the initial band gap is determined from the value between LUMO and HOMO of MoS_2 only (Figure 5.2(b)). Since LUMO of MoS_2 is lower than that of a-HfO_2, even though PDOS of MoS_2 is shifted to the right, the band gap is unchanged until the LUMO of MoS_2 coincides with that of a-HfO_2. Then after the electric field of 0.3 V/Å, the band gap is determined from the value between LUMO of a-HfO_2 and HOMO of MoS_2, and the band gap starts to decrease (see Figure 5.8(b) under the electric field of 0.20 and 0.50 V/Å, respectively).

From Figure 5.8, when PDOS of MoS_2 is shifted to the *n*-type or *p*-type directions, there are some additional states appearing at the edge of the original band gap region (around -1 eV under -0.15 V/Å and around 0.8 eV under 0.20 V/Å), resulting in decreasing the band gap of MoS_2. To clarify this behavior, we extract the band gap of only MoS_2 when the system (MoS_2 + pristine a-HfO_2) is under vertical electric field, and the results are shown in Figure 5.9. The trend of the band gap of MoS_2 with respect to different electric field is similar to that of the band gap of the whole system (MoS_2 + a-HfO_2) in Figure 5.7(b). When the negative electric field is increased, the band gap of MoS_2 is decreased instantly. On the other hand, under the positive electric field, the band gap of MoS_2 stays as its initial value at first, then starts to decrease significantly when the electric field is beyond 0.4 eV/Å. This result indicates that for the system of MoS_2 + a-HfO_2, the band gap of MoS_2 is highly affected depending on the direction and magnitude of the electric field, respectively.

5.4. Conclusion

In this study, we generated and investigated the band gap modulation of MoS_2 adsorbed on a-HfO_2 using MD and DFT simulations. The pristine a-HfO_2 decreases the band gap of adsorbed MoS_2 about 0.11 eV from its suspended structure. The defective sites on both structures showed that they can significantly modify the electronic properties of MoS_2. Introducing oxygen vacancy in a-HfO_2 decreases the band gap, and induces the *n*-type doping effect on MoS_2. As more defects are added, the reduction in the band gap becomes more. S-vacancy in MoS_2 can induce the finite state in the middle of the band gap, which decreases the band gap significantly (~ 0.7 eV). In addition, applied electric field significantly modulate the electronic properties of MoS_2 + a-HfO_2 structure. In particular, the band gap decreases as a larger value of electric field is applied. Depending on the direction of the electric field, MoS_2 becomes either *n*-type (under negative field) or *p*-type (under positive field), respectively. We believe that the study performed here can provide fundamental information on the structure and design considerations for the fabrication of electronic devices using MoS_2 such as FET and sensing devices.

5.5. Table and Figures

Structure	**Interlayer distance (Å)**	**Binding energy (eV)**
MoS_2 + a-HfO_2	1.91	2.96
MoS_2 + a-HfO_2 (VO)	1.69	6.94
MoS_2 + a-HfO_2 (2VO)	1.60	9.37
MoS_2 + a-HfO_2 (4VO)	1.57	11.43
MoS_2 (VS) + a-HfO_2	1.87	2.91
MoS_2 (VS) + a-HfO_2 (VO)	1.71	8.00
MoS_2 (VS + VMo) + a-HfO_2	1.81	3.26

Table 5.1: Interlayer distance and binding energy calculation for all configurations.

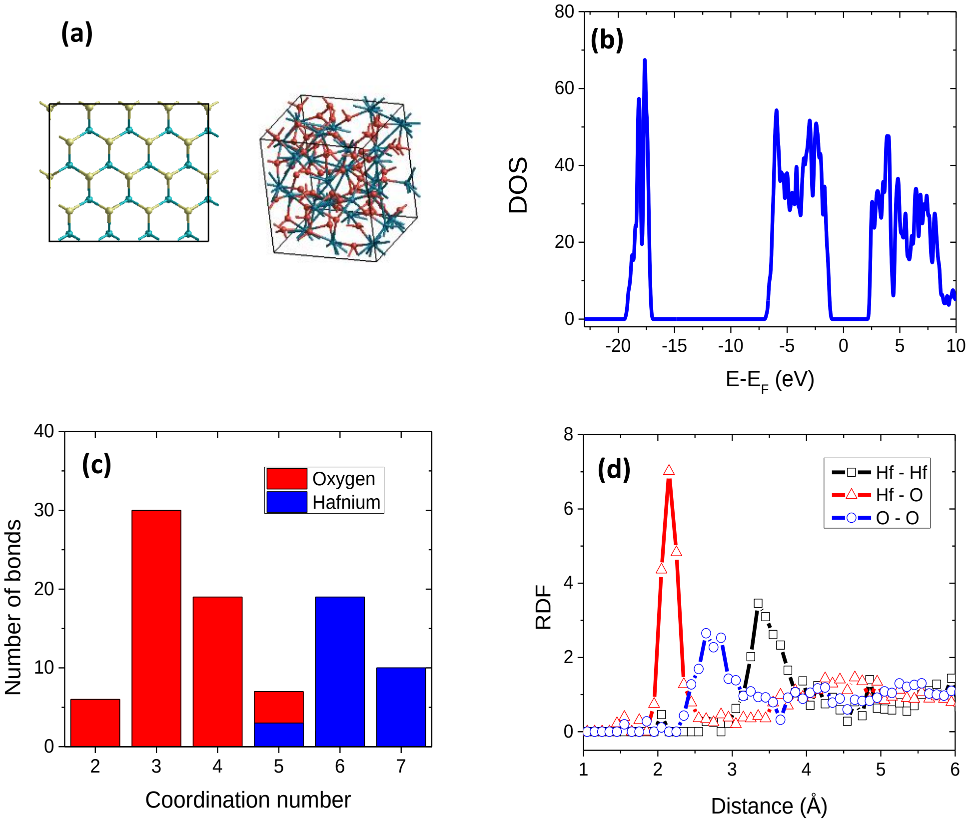

Figure 5.1: (a) Molecular snapshots for MoS_2 (left) and a-HfO_2 (right). Light blue, yellow, dark blue, and red color represent Mo, S, Hf, and O atom, respectively. (b) Density of states (DOS), (c) Coordination number, and (d) Radial distribution function (RDF) for a-HfO_2.

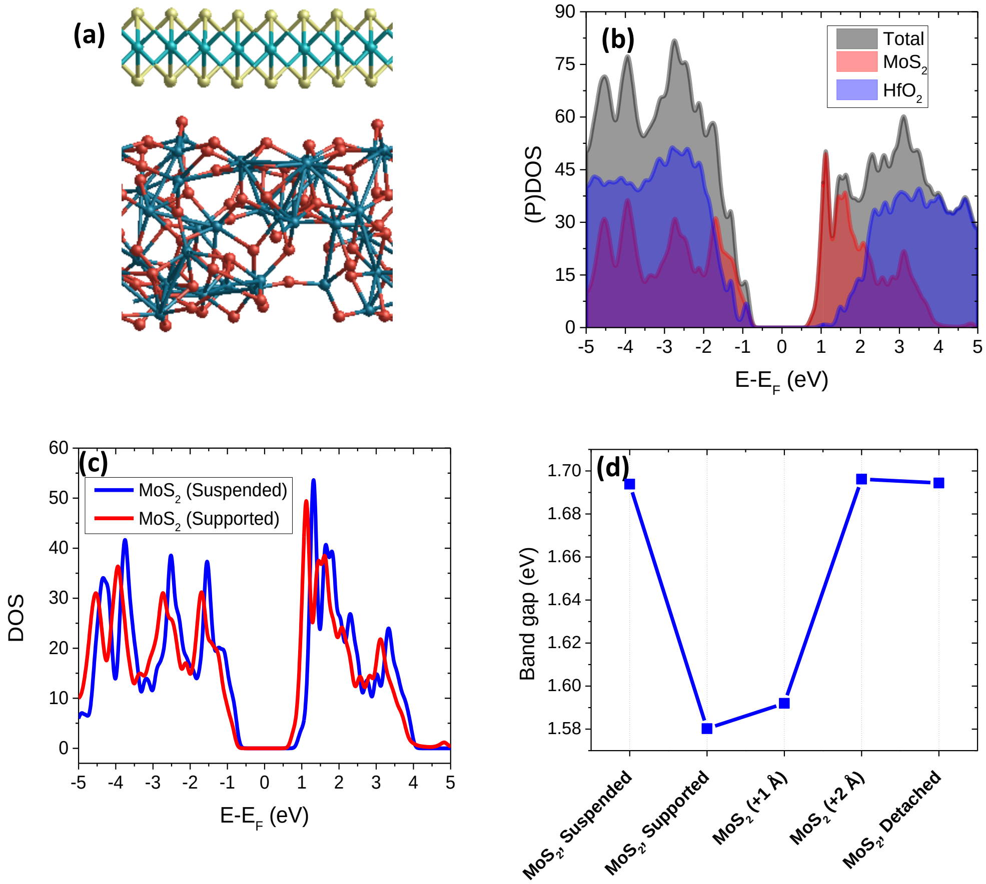

Figure 5.2: (a) Molecular snapshot of MoS_2 (top) deposited on a-HfO_2 (bottom). (b) Partial (PDOS) and total density of states (DOS) for MoS_2 on a-HfO_2. (c) DOS comparison between suspended and supported MoS_2. (d) Band gap change when the interlayer distance between two substrates is changed.

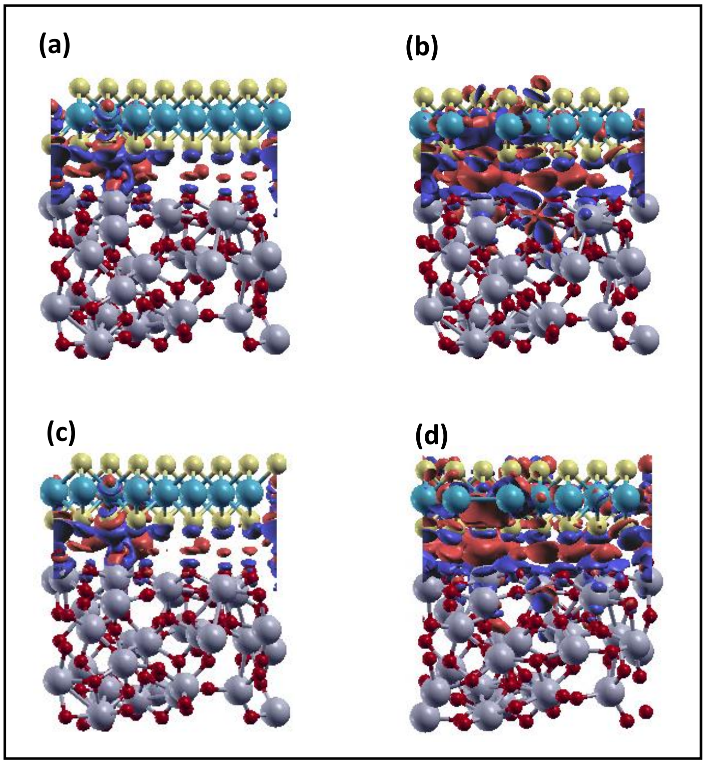

Figure 5.3: Charge density rearrangement ($\Delta\rho$) of (a) MoS_2 + a-HfO_2, (b) MoS_2 + a-HfO_2 (VO), (c) MoS_2 (VS) + a-HfO_2, and (d) MoS_2 (VS) + a-HfO_2 (VO). Red and blue isosurface represent charge accumulation and depletion region, respectively. Isosurface level is set to 0.0003 Å $^{-3}$.

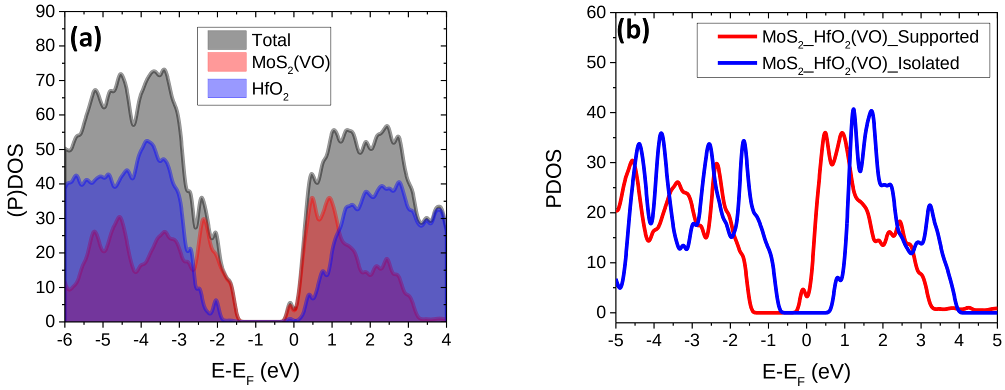

Figure 5.4: MoS_2 adsorbed on defective a-HfO_2 (VO) for (a) PDOS and DOS, and (b) PDOS comparison for supported and detached MoS_2.

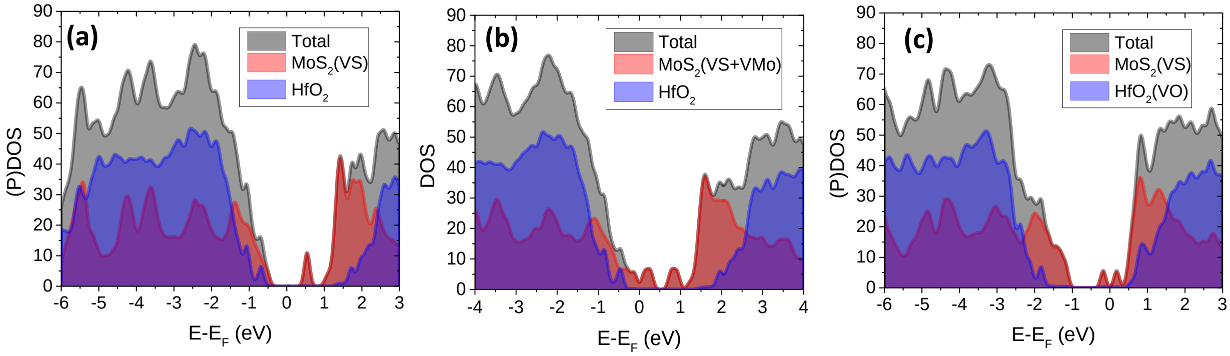

Figure 5.5: DOS and PDOS for (a) MoS_2 (VS) + a-HfO_2, (b) MoS_2 (VS + VMo) + a-HfO_2, and (c) MoS_2 (VS) + a-HfO_2 (VO).

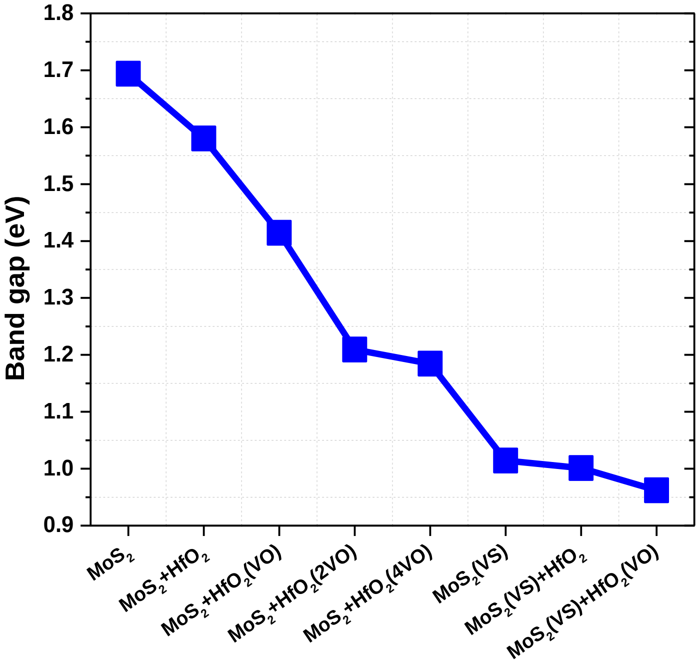

Figure 5.6: Band gap variation for all structure configurations of MoS_2 and a-HfO_2.

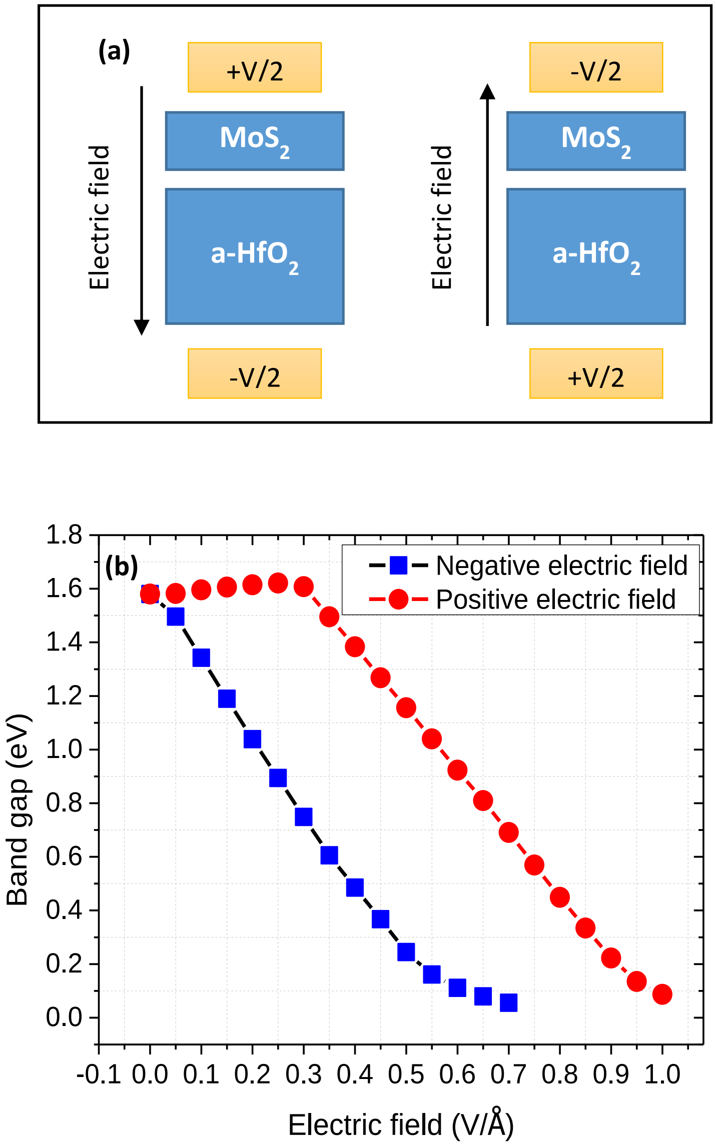

Figure 5.7: (a) Schematic view of MoS_2 + a-HfO_2 system under negative (Left) and positive (Right) vertical electric field. (b) Band gap change of MoS_2 + a-HfO_2 as a function of the electric field.

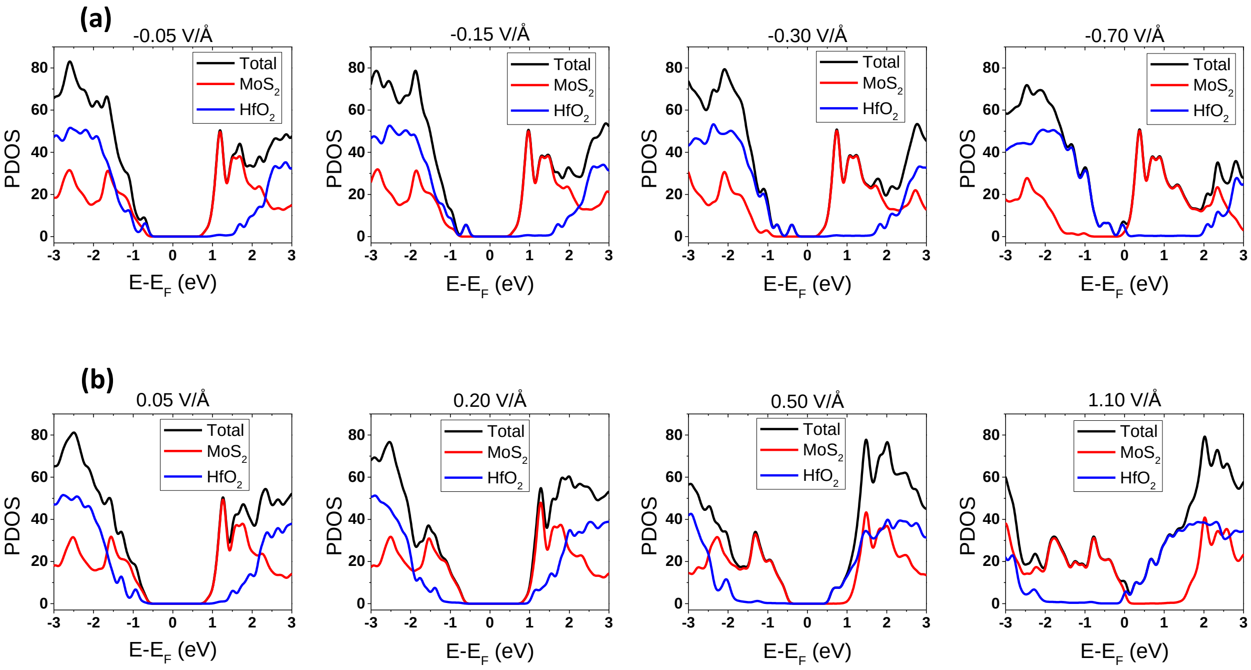

Figure 5.8: PDOS variation of MoS_2, a-HfO_2, and the whole system (MoS_2 + a-HfO_2) (a) under negative electric field with the strength of -0.05, -0.15, -0.30, and -0.70 eV/Å , respectively, and (b) under positive electric field with the strength of 0.05, 0.20, 0.50, and 1.10 eV/Å , respectively.

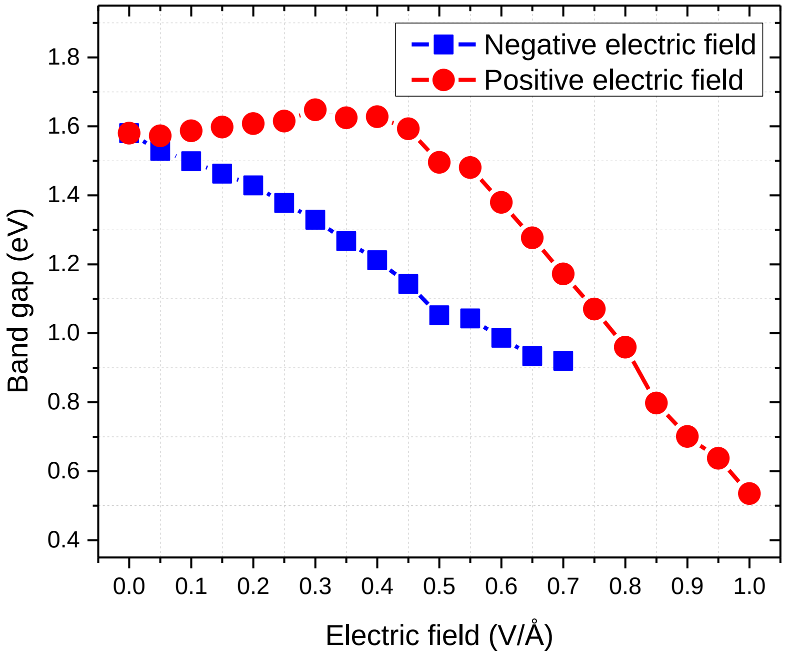

Figure 5.9: MoS_2 band gap variation as a function of the electric field.

CHAPTER 6

CONCLUSION

In this dissertation, the mechanical and electronic properties of nano-materials are investigated using quantum and atomistic simulation methods. We first employed the TB method and computed the mechanical properties of graphene under tension, and this result is compared to the MD simulation. Then by implementing DFT method, the mechanical properties of water filled C60 were studied. Water filled fullerene structures were further investigated with respect to the applied mechanical deformation and its effect on the electronic properties. A single-layer of MoS_2 was studied to examine how its electronic properties change when placed on a high k dielectric material (a-HfO_2) and the electric field effect was also investigated. The summary of each work follows.

Chapter 2 describes extensive study to understand the size and chirality effects on the elastic properties of graphene nanoribbons. The predicted Young's modulus for bulk graphene was in reasonable agreement with the published theoretical[9] and experimental[1] data. The stiffness decreased when the size of graphene nanoribbon decreased. Two dimensional graphene nanoribbons exhibited a larger size dependence on the mechanical properties compared to the one-dimensional carbon nanotubes.

In addition, the temperature and chirality dependent shear properties of graphene was investigated using MD simulations. Our results indicate that shear modulus increases up to around 800 K and decreases as the temperature is increased further. Shear strength and fracture strain decreased as the temperature increased. Zigzag graphene showed a higher shear modulus compared to the armchair structure. The shear fracture strength and shear fracture strain for the zigzag case were higher compared to the armchair case at lower temperatures, and no significant difference was observed at higher temperatures. We showed that analytical theory based on kinetic analysis compares reasonably with MD data. Finally, we investigated wrinkling of graphene under shear deformation since wrinkling can affect mechanical properties.

In Chapter 3, we described our study of the effect of encapsulated water molecules inside C60 on its mechanical properties using DFT calculations. The hydrostatic strain and point load conditions were considered under both tension and compression. The effect of water molecules on the mechanical behavior of C60 was clearly observed in all cases. Under tension, both loading conditions showed that the hydrostatic pressure at fracture and fracture stress decreased as more water molecules were added. Under compression, in contrast, structures could withstand more pressure (and stress) at the same strain with more water. This is because, as more water molecules are added in C60, internal pressure and interaction energy between the water and C60 increase. Fracture is initiated due to the bond formation between carbon and oxygen atoms under compression and bond-dissociation of carbon under tension. The results shown here suggest that water filled C60s can be good composite agents. Also, mechanical modulation of water filled C60 can be used to form new chemical compounds.

In Chapter 4, we investigated the effect of encapsulated water molecules inside fullerenes ($H_2O(n)$@C60, $H_2O(n)$@C180, and $H_2O(n)$@C240) on the variation of energy gap under mechanical deformation using DFT calculations. As with the C60, he point load was applied using both tension and compression. Also as with the C60, the effect of encapsulated water molecules was clearly observed in all the structures under compression. A clear variation of the energy gap was observed for all the water-filled fullerenes, compared to the empty fullerenes, as the applied compressive strain increased. This is due to the increase in the interaction energy between water molecules and the strained carbon wall. Unlike compression, no clear effect of water on the energy gap was observed under tension. This is because of the weak interaction between the water molecules and the fullerene wall.

In Chapter 5, the band gap modulation of MoS_2 adsorbed on a-HfO_2 was obtained using DFT simulation. The pristine a-HfO_2 decreased the band gap of adsorbed MoS_2 about 0.11 eV from its suspended structure. The defective sites on both substrates showed that they can significantly modify electronic properties. Introducing oxygen vacancy in a-HfO_2 decreased the band gap of MoS_2, and induced the *n*-type doping on MoS_2. As more defects were added, the reduction in band gap increased. We found that S-vacancy in MoS_2 can induce the finite state in the middle of band gap, which decreases the band gap significantly (~0.7 eV). In addition, applied electric field can significantly reduce the band gap depending on the direction of the field. We believe that this information can provide valuable information for design and fabrication of MoS_2 based FET and sensing devices.

REFERENCES

1. Lee, C.; Wei, X.; Kysar, J. W.; Hone, J. *Science* **2008,** 321, (5887), 385-388.
2. Radisavljevic, B.; Radenovic, A.; Brivio, J.; Giacometti, V.; Kis, A. *Nat. Nanotechnol.* **2011,** 6, (3), 147-150.
3. Soler, J. M.; Artacho, E.; Gale, J. D.; García, A.; Junquera, J.; Ordejón, P.; Sánchez-Portal, D. *Journal of Physics: Condensed Matter* **2002,** 14, (11), 2745.
4. Chenoweth, K.; van Duin, A. C.; Goddard, W. A. *The Journal of Physical Chemistry A* **2008,** 112, (5), 1040-1053.
5. Xu, C.; Wang, C.; Chan, C.; Ho, K. *Journal of Physics: Condensed Matter* **1992,** 4, (28), 6047.
6. Stuart, S. J.; Tutein, A. B.; Harrison, J. A. *The Journal of Chemical Physics* **2000,** 112, (14), 6472-6486.
7. Kurotobi, K.; Murata, Y. *Science* **2011,** 333, (6042), 613-616.
8. Frank, I.; Tanenbaum, D. M.; Van der Zande, A.; McEuen, P. L. *Journal of Vacuum Science & Technology B: Microelectronics and Nanometer Structures* **2007,** 25, (6), 2558-2561.
9. Liu, F.; Ming, P.; Li, J. *Physical Review B* **2007,** 76, (6), 064120.
10. Zhao, H.; Min, K.; Aluru, N. *Nano Letters* **2009,** 9, (8), 3012-3015.
11. Zhao, H.; Aluru, N. *Journal of Applied Physics* **2010,** 108, (6), 064321-064321-5.
12. Van Lier, G.; Van Alsenoy, C.; Van Doren, V.; Geerlings, P. *Chemical Physics Letters* **2000,** 326, (1), 181-185.
13. Blakslee, O. L.; Proctor, D. G.; Seldin, E. J.; Spence, G. B.; Weng, T. *Journal of Applied Physics* **1970,** 41, (8), 3373-3382.
14. Konstantinova, E.; Dantas, S. O.; Barone, P. M. V. B. *Physical Review B* **2006,** 74, (3), 035417.
15. Hernández, E.; Goze, C.; Bernier, P.; Rubio, A. *Physical Review Letters* **1998,** 80, (20), 4502-4505.
16. Gupta, S.; Dharamvir, K.; Jindal, V. K. *Physical Review B* **2005,** 72, (16), 165428.
17. WenXing, B.; ChangChun, Z.; Wanzhao, C. *Physica B: Condensed Matter* **2004,** 352, (1), 156-163.
18. Chang, T.; Gao, H. *Journal of the Mechanics and Physics of Solids* **2003,** 51, (6), 1059-1074.
19. Sakhaee-Pour, A. *Solid State Communications* **2009,** 149, (1), 91-95.
20. Zakharchenko, K.; Katsnelson, M.; Fasolino, A. *Physical Review Letters* **2009,** 102, (4), 046808.
21. Tsai, J.-L.; Tu, J.-F. *Materials & Design* **2010,** 31, (1), 194-199.
22. McSkimin, H.; Andreatch, P. *Journal of Applied Physics* **1972,** 43, (7), 2944-2948.
23. Roundy, D.; Cohen, M. L. *Physical Review B* **2001,** 64, (21), 212103.
24. Zhang, Y.; Sun, H.; Chen, C. *Physical Review Letters* **2004,** 93, (19), 195504.
25. Lu, J. P. *Physical Review Letters* **1997,** 79, (7), 1297-1300.
26. Hall, A. R.; An, L.; Liu, J.; Vicci, L.; Falvo, M. R.; Superfine, R.; Washburn, S. *Physical Review Letters* **2006,** 96, (25), 256102.
27. Lu, J.; Zhang, L. *Computational Materials Science* **2006,** 35, (4), 432-441.
28. Wong, Y. W.; Pellegrino, S. *J. Mech. Mater. Struct* **2006,** 1, (1), 1-23.

29. Wang, C. Y.; Mylvaganam, K.; Zhang, L. C. *Physical Review B* **2009,** 80, (15), 155445.
30. Horsfield, A. P. *Materials Science and Engineering: B* **1996,** 37, (1–3), 219-223.
31. Wallace, D. C., *Thermodynamics of crystals*. DoverPublications. com: 1998.
32. Reddy, C.; Rajendran, S.; Liew, K. *Nanotechnology* **2006,** 17, (3), 864.
33. Brenner, D. W. *Physical Review B* **1990,** 42, (15), 9458-9471.
34. Plimpton, S. *Journal of Computational Physics* **1995,** 117, (1), 1-19.
35. Belytschko, T.; Xiao, S. P.; Schatz, G. C.; Ruoff, R. S. *Physical Review B* **2002,** 65, (23), 235430.
36. Zhurkov, S. *Int. J. Fract. Mech* **1965,** 1, 311-323.
37. Bailey, J. *Glass Industry* **1939,** 20, 26.
38. Wong, W.; Pellegrino, S. *Journal of Mechanics of Materials and Structures* **2006,** 1, (1), 27-61.
39. Pupysheva, O. V.; Farajian, A. A.; Yakobson, B. I. *Nano Letters* **2007,** 8, (3), 767-774.
40. Weidinger, A.; Waiblinger, M.; Pietzak, B.; Murphy, T. A. *Applied Physics A* **1998,** 66, (3), 287-292.
41. Ensing, B.; Costanzo, F.; Silvestrelli, P. L. *Journal of Physical Chemistry A* **2012,** 116, (49), 12184-12188.
42. Farimani, A. B.; Wu, Y.; Aluru, N. *Physical Chemistry Chemical Physics* **2013**.
43. Ruoff, R. S.; Ruoff, A. L. *Applied Physics Letters* **1991,** 59, (13), 1553-1555.
44. Cai, J.; Bie, R.; Tan, X.; Lu, C. *Physica B: Condensed Matter* **2004,** 344, (1), 99-102.
45. Min, K.; Aluru, N. *Applied Physics Letters* **2011,** 98, (1), 013113-013113-3.
46. Adnan, A.; Sun, C.; Mahfuz, H. *Composites Science and Technology* **2007,** 67, (3), 348-356.
47. Li, Y. *Polymer* **2011,** 52, (10), 2310-2318.
48. Shen, H. *Materials Letters* **2006,** 60, (16), 2050-2054.
49. Kohn, W.; Sham, L. J. *Physical Review* **1965,** 140, (4A), A1133-A1138.
50. Perdew, J. P.; Zunger, A. *Physical Review B* **1981,** 23, (10), 5048-5079.
51. Perdew, J. P.; Wang, Y. *Physical Review B* **1992,** 45, (23), 13244-13249.
52. Perdew, J. P.; Burke, K.; Ernzerhof, M. *Physical Review Letters* **1996,** 77, (18), 3865-3868.
53. Hammer, B.; Hansen, L. B.; Nørskov, J. K. *Physical Review B* **1999,** 59, (11), 7413-7421.
54. Perdew, J. P.; Ruzsinszky, A.; Csonka, G. I.; Vydrov, O. A.; Scuseria, G. E.; Constantin, L. A.; Zhou, X.; Burke, K. *Physical Review Letters* **2008,** 100, (13), 136406.
55. Becke, A. D. *The Journal of Chemical Physics* **1993,** 98, (7), 5648-5652.
56. Hamann, D. R.; Schlüter, M.; Chiang, C. *Physical Review Letters* **1979,** 43, (20), 1494-1497.
57. Dumitrică, T.; Belytschko, T.; Yakobson, B. I. *Journal of Chemical Physics* **2003,** 118, 9485.
58. Leu, P. W.; Svizhenko, A.; Cho, K. *Physical Review B* **2008,** 77, (23), 235305.
59. Topsakal, M.; Ciraci, S. *Physical Review B* **2010,** 81, (2), 024107.
60. Ye, W.; Min, K.; Martin, P. P.; Rockett, A. A.; Aluru, N.; Lyding, J. W. *Surface Science* **2012**.
61. Kumar, B.; Min, K.; Bashirzadeh, M.; Farimani, A. B.; Bae, M.-H.; Estrada, D.; Kim, Y. D.; Yasaei, P.; Park, Y. D.; Pop, E. *Nano Letters* **2013,** 13, (5), 1962-1968.
62. Troullier, N.; Martins, J. L. *Physical Review B* **1991,** 43, (3), 1993-2006.
63. Valentini, P.; Gerberich, W.; Dumitrică, T. *Physical Review Letters* **2007,** 99, (17), 175701.
64. Ramachandran, C.; Sathyamurthy, N. *Chemical Physics Letters* **2005,** 410, (4), 348-351.
65. Zhang, Q. M.; Yi, J.-Y.; Bernholc, J. *Physical Review Letters* **1991,** 66, (20), 2633-2636.
66. Xie, R.-H.; Bryant, G. W.; Jensen, L.; Zhao, J.; Smith Jr, V. H. *Journal of Chemical Physics* **2003,** 118, 8621.
67. Barati Farimani, A.; Aluru, N. *Journal of Physical Chemistry B* **2011,** 115, (42), 12145-12149.
68. Min, K.; Farimani, A. B.; Aluru, N. *Applied Physics Letters* **2013,** 103, (26), 263112.
69. Farimani, A. B.; Wu, Y.; Aluru, N. *Physical Chemistry Chemical Physics* **2013,** 15, (41), 17993-18000.
70. Rivelino, R.; de Brito Mota, F. *Nano Letters* **2007,** 7, (6), 1526-1531.

71. Kawahara, S. L.; Lagoute, J.; Repain, V.; Chacon, C.; Girard, Y.; Rousset, S.; Smogunov, A.; Barreteau, C. *Nano Letters* **2012,** 12, (9), 4558-4563.
72. Ni, Z. H.; Yu, T.; Lu, Y. H.; Wang, Y. Y.; Feng, Y. P.; Shen, Z. X. *ACS Nano* **2008,** 2, (11), 2301-2305.
73. Yang, L.; Anantram, M.; Han, J.; Lu, J. *Physical Review B* **1999,** 60, (19), 13874.
74. Scalise, E.; Houssa, M.; Pourtois, G.; Afanas'ev, V.; Stesmans, A. *Nano Res.* **2012,** 5, (1), 43-48.
75. Farimani, A. B.; Min, K.; Aluru, N. R. *ACS Nano* **2014**.
76. Calaminici, P.; Geudtner, G.; Köster, A. M. *Journal of Chemical Theory and Computation* **2008,** 5, (1), 29-32.
77. Zope, R. R.; Baruah, T.; Pederson, M. R.; Dunlap, B. *Physical Review B* **2008,** 77, (11), 115452.
78. Li, T. *Physical Review B* **2012,** 85, (23), 235407.
79. Li, J.; Medhekar, N. V.; Shenoy, V. B. *The Journal of Physical Chemistry C* **2013,** 117, (30), 15842-15848.
80. Li, Y.; Zhou, Z.; Zhang, S.; Chen, Z. *Journal of the American Chemical Society* **2008,** 130, (49), 16739-16744.
81. Ataca, C.; Şahin, H.; Aktürk, E.; Ciraci, S. *The Journal of Physical Chemistry C* **2011,** 115, (10), 3934-3941.
82. Liu, D.; Guo, Y.; Fang, L.; Robertson, J. *Applied Physics Letters* **2013,** 103, (18), -.
83. Farimani, A. B.; Min, K.; Aluru, N. R. *ACS nano* **2014,** 8, (8), 7914-7922.
84. Conley, H. J.; Wang, B.; Ziegler, J. I.; Haglund, R. F.; Pantelides, S. T.; Bolotin, K. I. *Nano Letters* **2013,** 13, (8), 3626-3630.
85. Scopel, W. L.; Fazzio, A.; Miwa, R. H.; Schmidt, T. M. *Physical Review B* **2013,** 87, (16), 165307.
86. Ryu, S.; Liu, L.; Berciaud, S.; Yu, Y.-J.; Liu, H.; Kim, P.; Flynn, G. W.; Brus, L. E. *Nano Letters* **2010,** 10, (12), 4944-4951.
87. Dolui, K.; Rungger, I.; Sanvito, S. *Phys. Rev. B* **2013,** 87, (16), 165402.
88. Fallahazad, B.; Kim, S.; Colombo, L.; Tutuc, E. *Applied Physics Letters* **2010,** 97, (12), -.
89. Gutiérrez, G.; Johansson, B. *Physical Review B* **2002,** 65, (10), 104202.
90. Shan, T.-R.; Devine, B. D.; Hawkins, J. M.; Asthagiri, A.; Phillpot, S. R.; Sinnott, S. B. *Physical Review B* **2010,** 82, (23), 235302.
91. Shan, T.-R.; Devine, B. D.; Kemper, T. W.; Sinnott, S. B.; Phillpot, S. R. *Physical Review B* **2010,** 81, (12), 125328.
92. Chen, T.-J.; Kuo, C.-L. *Journal of Applied Physics* **2011,** 110, (6), 064105.
93. Monkhorst, H. J.; Pack, J. D. *Physical Review B* **1976,** 13, (12), 5188-5192.
94. Ataca, C.; Sahin, H.; Akturk, E.; Ciraci, S. *The Journal of Physical Chemistry C* **2011,** 115, (10), 3934-3941.
95. Xu, M.; Liang, T.; Shi, M.; Chen, H. *Chemical Reviews (Washington, DC, United States)* **2013,** 113, (5), 3766-3798.
96. Galup-Montoro, C., *MOSFET modeling for circuit analysis and design*. World scientific: 2007.
97. Yue, Q.; Chang, S.; Kang, J.; Zhang, X.; Shao, Z.; Qin, S.; Li, J. *Journal of Physics: Condensed Matter* **2012,** 24, (33), 335501.
98. Ramasubramaniam, A.; Naveh, D.; Towe, E. *Physical Review B* **2011,** 84, (20), 205325.
99. Qi, J.; Li, X.; Qian, X.; Feng, J. *Applied Physics Letters* **2013,** 102, (17), 173112.
100. Mulliken, R. S. *The Journal of Chemical Physics* **1955,** 23, (10), 1833-1840.
101. Stuart, S. J.; Tutein, A. B.; Harrison, J. A. *The Journal of Chemical Physics* **2000,** 112, 6472.
102. Wu, Y.; Aluru, N. R. *The Journal of Physical Chemistry B* **2013,** 117, (29), 8802-8813.

APPENDIX A

A.1 Density of states (DOS) and HOMO-LUMO energy

The density of states (DOS, $D(E)$) is the number of available energy (E) levels or states per energy step (dE) (between E and E + dE) in the electronic systems. This is one of the fundamental electronic properties for description of metals, semi-metal, semiconductors, and insulators. DOS can be defined as:

$$D(E) = \frac{dNs}{dE} \tag{A.1}$$

where Ns is the total number of energy states in the system, dE is the size of the energy step, and $\int_1^N D(E)dE$ = the total number of basis orbitals in the system.

From the DFT calculation, one can obtain all of the Hamiltonian eigenvalues of the system by solving the KS equation, and DOS can be calculated from them. Similarly, the local density of states (LDOS) can be determined by obtaining the electron density at point r. Summing up LDOS over all atoms gives the DOS. The DOS of graphene is shown as an example in Figure A.2.

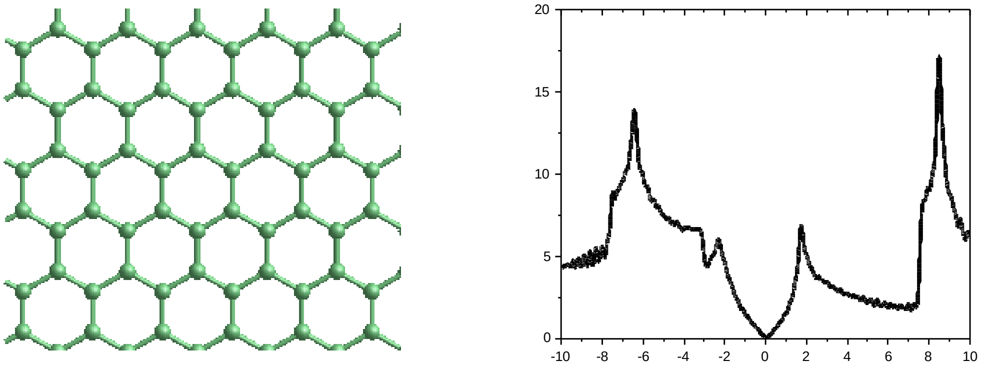

Figure A.1: (Left) The structure of the single-layer of graphene. (Right) Density of states (DOS) of graphene

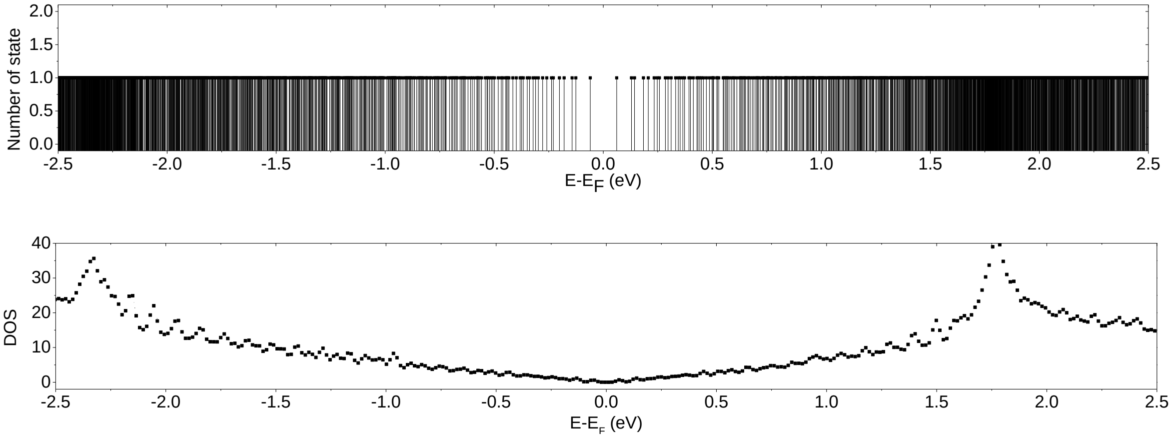

Figure A.2: (Top) The number of states (eigenvalues) vs. energy in graphene. (Bottom) Density of states of graphene from the number of states by using Eq. (A.1).

In addition, one can obtain the highest occupied molecular orbital (HOMO) and lowest unoccupied molecular orbital (LUMO) energy of the system from the KS eigenvalue calculation. For example, graphene consisting of 96 carbon atoms has 1248 energy states which is calculated as 96 (number of atoms) × 13 (number of orbitals from the localized orbital basis set generation using DZP). Since the valance of carbon is 4 ($2s^2+2p^2$), total valance charge per spin of graphene is 4×96/2 = 192. This means the HOMO and LUMO energy of graphene is 192nd and 193rd eigenvalue from the lowest (smallest) eigenvalue, respectively.

A.2 Electron (Charge) density

In quantum chemical calculations, the electron (charge) density, $n(\vec{r})$, is the probability of an electron occupation at the coordinates ($\vec{r}$). Since the electronic wavefunctions are solved through the KS equation, the electron density matrix can be constructed by the following steps:

When one substitutes the wavefunction, $\psi_i(\vec{r}) = \sum_{\alpha}^{M} c_{i\alpha}\phi_\alpha(\vec{r})$, into the electron density, $n(\vec{r}) = \sum_{i}^{N} f_i \left|\psi_i(\vec{r})\right|^2$, the equations becomes

$$n(\vec{r}) = \sum_{\alpha\beta} n_{\alpha\beta}\phi_\beta^*(\vec{r})\phi_\alpha(\vec{r}) \tag{A.2}$$

where $c_{i\alpha} = \langle \tilde{\phi}_\alpha | \psi_i \rangle$, and $\tilde{\phi}_\alpha$ are the dual orbital of $\phi_\alpha : \langle \tilde{\phi}_\alpha | \phi_\beta \rangle = \delta_{\alpha\beta}$. Then with $c_{i\beta} = c_{\beta i}^*$, the electron density matrix can be rewritten as:

$$n_{\alpha\beta} = \sum_i c_{\alpha i} f_i c_{i\beta} \tag{A.3}$$

To obtain the electron density at a specific grid point, atomic orbitals are first obtained from the basis set generation, then they are interpolated.

The electron (charge) density can be used to describe the electron cloud overlap behavior when molecules are interacting with certain materials. As an example, the electron density difference for water-encapsulated C60 ($H_2O(1)@C60$) is shown in Figure A.3. The electron density difference ($\Delta\rho$) is calculated as $\Delta\rho = \rho_{C60+Water} - (\rho_{C60} + \rho_{Water})$, where ρ_{C60} and ρ_{Water} represent the charge density distribution of each structure (fullerene and water), and $\rho_{C60+Water}$ is the charge density distribution of the total system.

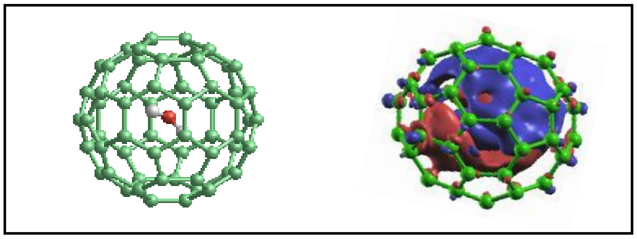

Figure A.3: (Left) Molecular snapshot of water encapsulated C60. (Right) 3D charge density rearrangement ($\Delta\rho$) of water-filled fullerenes. (Red and blue isosurface represent charge accumulation and depletion, respectively.)

APPENDIX B

B.1 Issue in applying compression using DFT

In order to compare the mechanical behavior of water filled C60 under different loading conditions (i.e. point load, and contact compressive loading), we considered two cases of C60 and $H_2O(1)C60$ between two plates to mimic the contact compressive loading condition. In these types of simulations (contact compressive loading), two plates (made of graphene) are placed at a small distance of 2 Å from C60 (see Figure B.1). MD simulation is performed using LAMMPS. To compare the effect of the choice of the potential, we used two different potentials: 1.AIREBO (for C-C interaction) with water-carbon force-field developed in our group and 2. ReaxFF potential (for C, H and O).[4, 101, 102] The initial setup for MD is shown in Figure B.1. In the case of water filled C60, water is placed in the center of C60. To compress the C60, a strain increment of 0.0076 is applied to the plates, and then the energy minimization of the system is performed while fixing the atomic coordinates of the plates in all the directions.

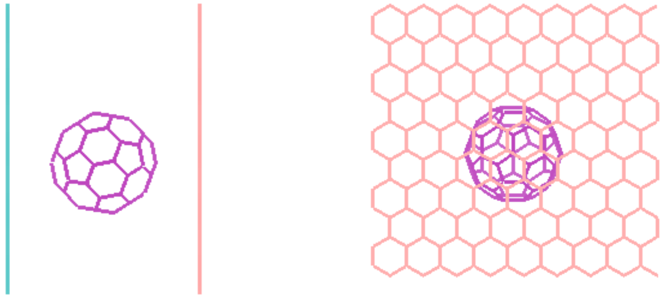

Figure B.1: System setup (top view (left) and side view (right)) for applying compression using two plates.

B.2 Comparison between DFT and MD

Based on the strain energy variation shown in Figure B.2, all three methods (point load, two plates with AIREBO and two plates with Reaxff) are comparable up to around a strain of 0.25. Beyond that, the energy variation depends on the method employed. It should be noted that in the case of compression with two plates, there is an extensive deformation distributed on the surface of sphere compared to the point load case (see, for example, snapshots at 0.45 strain in Figure B.2). Under point load the applied load is more concentrated on the middle of the sphere at 0.45 and 0.6 strains. It should be noted that the point load also deforms the surface area but not as significantly as the two plates case (Figure B.3).

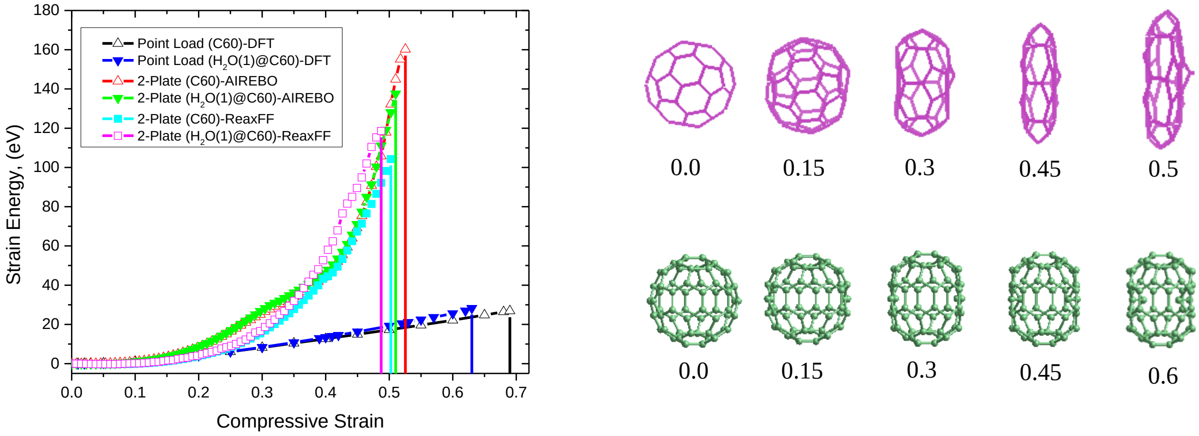

Figure B.2: (Left) Variation of strain energy with compressive strain for C60 and $H_2O(1)@C60$ using the two plates approach (MD with AIREBO and ReaxFF) and the point load approach (DFT). (Right) Molecular snapshots of C60 at each strain under compression using the two plates approach (top) with AIREBO potential and the point load approach using DFT.

Based on our observations, using the point load within DFT scheme can reasonably capture the mechanical properties of water inside C60 due to following reasons: First, the potentials available for MD simulations are not verified for mechanical properties, especially for interaction between water and C60. The water-carbon interaction force-field cannot capture the bond-formation and the bond-breaking which are key factors in fracture of water-filled buckyball under deformation.[102] In the case of ReaxFF potential, this has not been adequately studied to understand if it can capture the interaction between buckyball and water, and mechanical properties under various loading conditions. Second, it is difficult to perform loading/strain with two plates using DFT because of the limited number of atoms DFT can deal with (the two plates includes about 433 atoms). Finally, it is not clear if the tensile case can be studied easily using two plates, hence the results in the main text contain only the point load case.

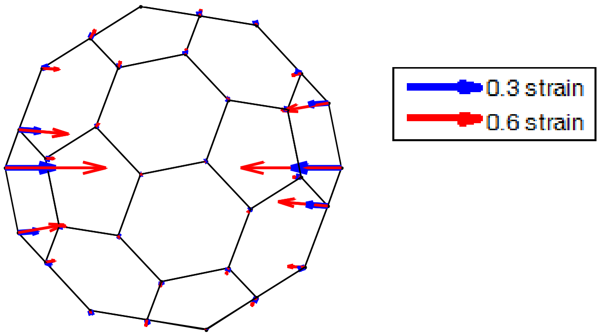

Figure B.3: Displacement vector of C60 at each applied strain with respect to its initial position.